STUDY OF KINEMATICS AND CHEMICAL ABUNDANCES PROPERTIES OF DAMPED AND SUB-DAMPED LYMAN ALPHA QUASAR ABSORBERS FROM THE SLOAN DIGITAL SKY SURVEY

A FINAL REPORT OF MINI-RESEARCH SUBMITTED TO
DEAN'S OFFICE
INSTITUTE OF SCIENCE AND TECHNOLOGY
TRIBHUVAN UNIVERSITY
KIRTIPUR, NEPAL

BY
YOGESH SINGH MAHARJAN
DEPARTMENT OF PHYSICS
AMRIT SCIENCE CAMPUS
THAMEL
MAY 2024

DECLARATION

This mini project work entitled **"Study of kinematics and chemical abundances properties of Damped and Sub-Damped Lyman alpha quasar absorbers from the Sloan Digital Sky Survey"** is being submitted to the Mini Research Grant to Institute of Science and Technology (IoST), Tribhuvan University, Kirtipur, Nepal for the progress update requirement. This mini research is carried through under the guidance of Assoc. Prof. Dr. Niraj Dhital in the Central Department of Physics, Tribhuvan University (T.U.), Kirtipur, Kathmandu.

This research is original and has never before been submitted in whole or in part, in any format, to any university or institute, domestically or abroad, for the purpose of conferring a degree.

.....

Mr. Yogesh Singh Maharjan
Assistant Professor
Department of Physics
Amrit Campus,TU
Nepal

RECOMMENDATION

This is to recommend that **Asst. Prof. Yogesh Singh Maharjan** of Department of Physics, Amrit Campus, Tribhuvan University**,** has carried out mini research project work entitled **"Study of kinematics and chemical abundances properties of Damped and Sub-Damped Lyman alpha quasar absorbers from the Sloan Digital Sky Survey".**

This work hasn't been submitted for any other degree, as far as I know.

He complies with all the standards set forth by the Mini Research Grant to Institute of Science and Technology (IoST), Tribhuvan University, Kirtipur, Nepal for the submission of the progress update requirement of this mini project work.

.....

Dr. Niraj Dhital
Supervisor
Associate Professor
Central Department of Physics, TU
Kathmandu, Nepal

MAY 2024

ACKNOWLEDGEMENTS

My deepest appreciation goes out to my supervisors, Assoc. Prof. Niraj Dhital and Dr. Suraj Poudel for invaluable support, encouragement, and guidance in every part of this study. I am thankful to Mini Research Grant to Institute of Science and Technology (IoST), Tribhuvan University, Kirtipur, Nepal for providing me grant to conduct this research entitled " **Study of kinematics and chemical abundances properties of Damped and Sub-Damped Lyman alpha quasar absorbers from the Sloan Digital Sky Survey**."

Once again, I'm grateful and feel awesome to have best friend and mentor Dr. Suraj Poudel, who's guidance and introduce to this subject matter help me to understand beauty of evolution of galaxies in early universe epoch.

I extend my heartfelt appreciation to my wife Mrs. Manju Sukhupayo, daughter Ms. Myra Singh Maharjan and parents for their unwavering compassion, prayers, belief, and motivation throughout my research work. They provided emotional assistance, and I am truly grateful for their presence.

Mr. Yogesh Singh Maharjan
Assistant Professor
Department of Physics
Amrit Campus, TU
Nepal
(May, 2024)

शोध सार

तारापुञ्जहरुको उत्पत्ति र विकासको बारेमा बुझ्नको लागि तारापुञ्जहरुमा उपलब्ध धातु र ग्याँसहरुको बारेमा अध्ययन गर्नु निकै महत्वपूर्ण हुन्छ । धेरै मधुरो हुने भएकोले उच्च redshift भएका तारापुञ्जहरुको emission-line प्रविधिबाट अध्ययन गर्न नसकिने हुन्छ । यद्यपि absorption मा भने यी तारापुञ्जहरुको अवलोकन गर्न सकिन्छ । सामान्यत अग्रभूमिमा रहेका तारापुञ्जहरुको अध्ययन गर्नको लागि पृष्ठभूमिमा रहेका quasar हरुको प्रयोग गरिन्छ । Quasar हरुको spectra मा भएका absorption line हरुलाई तारापुञ्जहरु वरिपरि रहेका ग्याँसहरुको गुणहरुको बारेमा अध्ययन गर्ने प्रभावकारी तथा चमक-निरपेक्ष (luminosity-independent) तरिका हुन सक्छ । यसलाई तारापुञ्जहरु, circumgalactic medium (CGM) तथा intergalactic medium (IGM) को बारेमा अध्ययन गर्नको लागि प्रयोग गरिएका छन् । यद्यपि, quasar हरुको उच्च रेजोलुसनका spectroscopic अवलोकन निकै खर्चिलो हुन्छ भने Sloan Digital Sky Survey (SDSS) जस्ता पूर्णआकाशीय सर्वेक्षणहरुबाट प्राप्त कम रेजोलुसनका डाटा भने सार्वजनिक रुपमा पाइन्छन् । यस अध्ययनका लागि हामीले उच्च मात्रामा ग्याँस उपलब्ध भएका तारापुञ्जहरुको kinematics तथा रसायनिक गुणहरुको पहिचान तथा अध्ययनका लागि उच्च redshift भएका तारापुञ्जहरुको SDSS सर्वेक्षणबाट प्राप्त सयौँ spectra हरुको प्रयोग गरेका छौँ ।

यस रिपोर्टमा $3 \lesssim z_{abs} \lesssim 5$ को खगोलीय redshift ले छोडेको तारापुञ्जको विकासको छापको अध्ययन गर्न DLA तथा sub-DLA quasar absorber हरुको chemical abundance measurement प्रस्तुत गरिएको छ । हामीले neutral hydrogen column density $\log N_{H\,I}$ (cm^{-2}) = 20.55 ± 0.2, 20.34 ± 0.2, 20.35 ± 0.2 भएका ३ नयाँ DLA हरु र neutral hydrogen column densities $\log N_{H\,I}$ (cm^{-2}) = 20.1 ± 0.2, 20.25 ± 0.2, 20.1 ± 0.2 भएका ३ नयाँ sub-DLA हरु पत्ता लगाएका छौँ जसमा $3\,\sigma$ भन्दा बढीमा थुप्रै ion हरु पत्ता लागेका छन् । धेरै ग्याँस भएका यी ६ वटा तारापुञ्जहरुमा पृष्ठभूमिमा रहेका Quasar हरुको Lyman α absorption उच्च देखिन्छ जसमा २ वटा sightline हरुले धातु बढी भएका र बाँकी ४ वटाले धातु कम भएका तारापुञ्जहरुको अध्ययन गरेका थिए । हामीले VoigFit प्रोग्रामसँग मेल खाने Voigt profile को प्रयोग गरेर H I column density को निर्धारण गरेका थियौँ । हामीले Linetools नामक spectra को विश्लेषण गर्ने टुलको मद्दतबाट Apparent Optical Depth (AOD) विधि अपनाई र Gaussian सँग मिलाएर equivalent widths तथा metal column densities को थप आंकलन गरेका थियौँ । हामीले [C/O] तथा [Si/O] को तुलनात्मक प्रचुरताको अध्ययन गर्दा ६ वटामध्ये २ वटा प्रणालीहरुमा सौर्यमण्डलकै अनुपातमा (solar ratio) र बाँकीमा सौर्यमण्डलभन्दा प्रचुर अनुपातमा (super solar ratio) रहेको पायौँ । यसले प्राचीन ताराहरुबाट पाएको भन्ने संकेत गर्दछ । हामीले kinematics को अध्ययनको लागि velocity dispersion को पनि मापन गर्‍यौँ । हामीले C IV र Si IV को अवशोषणको पनि संकेत पायौँ जसले यी DLA/sub-DLA हरुमा collisional ionization को अस्तित्वको संकेत गर्छ । N (C IV)/N (Si IV) को column density ratio हरु १.४ देखि ६.५ भित्र परेको देखिएबाट यी absorber हरु photoionization र collisional ionization दुबै प्रक्रियाबाट ionize भएको हो भन्ने संकेत गर्दछ ।

Key Words: quasars: absorption lines, Cosmos history, ISM: abundances, redshift

ABSTRACT

Studying the lifecycle of metals and gas in a galaxy is important to understand the formation and development of Galaxies. Galaxies at high redshifts are very faint to study in emission-line technique, but can be observed in absorption. Generally, background quasars are utilized to study the galaxies in the foreground. Quasar absorption lines serve as valuable tools for studying features of gas within and surrounding galaxies. These lines are independent of quasar luminosity and have been widely employed in the study of galaxies, IGM and CGM. However, getting the high-resolution spectroscopic observation of quasars is very expensive, meanwhile, low resolution data from the all-sky survey such as SDSS are publicly available. For this research, we utilize hundreds of spectra from the SDSS with galaxies of high-redshift to identify, study the kinematic and chemical properties of the gas-rich galaxies (Damped Lyman-alpha systems).

The report introduces measurements chemical abundance of DLAs and sub-DLAs quasar absorbers galaxy evolution traced by at cosmological redshift of $3 \lesssim z_{abs} \lesssim 5$. We found 3 new DLAs with neutral hydrogen column densities log $N_{H\,I}$ (cm^{-2}) = 20.55 $\pm$ 0.2, 20.34 $\pm$ 0.2, 20.35 $\pm$ 0.2 and 3 new sub-DLAs with neutral hydrogen column densities log $N_{H\,I}$ (cm^{-2}) = 20.1$\pm$ 0.2, 20.25 $\pm$ 0.2, 20.1 $\pm$ 0.2 with multiple ions detected at more than 3 σ. These 6 new gas-rich galaxies show strong Lyman α absorption in the background Quasars with 2 sightlines probing metal rich and remining 4 probing metal poor galaxies. We determined H I column density using Voigt profile fitting program VoigtFit. We further estimate the equivalent widths and metal column densities fitting the Gaussian and applying the Apparent Optical Depth (AOD) method with the help of spectra analysis tool called Linetools. We further studied the relative abundance of [C/O] and [Si/O] and found that two out of six systems have solar and other have super-solar ratios which may signify the enrichment from early stars. We also measure the velocity dispersion to study the kinematics. We also detect C IV and Si IV absorption signifying that the collisional ionization may be prevalent in these DLAs/sub-DLAs. The column density ratios of N (C IV)/N (Si IV) in the range of in the range of 1.4 – 6.5, signifying these absorbers may be ionized by both the photoionization and collisional ionization.

Key Words: quasars: absorption lines, Cosmos history, ISM: abundances, redshift

LIST OF ACRONYMS AND ABBREVIATIONS

AOD	Apparent Optical Depth
CGM	Circumgalactic Medium
Dex	decimal exponent
DLA	Damped Lyman-α
FITS	Flexible Image Transport System Image File
IGM	Intergalactic Medium
ISM	Interstellar Medium
LLS	Lyman Limit System
Ly-α	Lyman Alpha
QSO	Quasi Steller Object (Quasar)
SDSS	Sloan Digital Sky Survey
sub-DLA	Sub-Damped Lyman-α
UV	Ultra Violet

LIST OF SYMBOLS

e	Electron
K	Kelvin
$M_{\odot}$	Solar Mass
MeV	Mega Electron Volt
N	Column Density
n	Neutron
p	Proton
W	Equivalent Width
Z	Atomic Number
z_{abs}	Red Shift of absorber
z_{qso}	Red Shift of QSO
α	Alpha
λ	Wavelength
σ	Standard Deviation
υ_e	Neutrino

LIST OF TABLES

Table 3.1 Classification of Ly-α system based on column density (Péroux et al. 2003)..... 15
Table 3.2 Element Composition of solar photosphere elements (Asplund et al. 2009)..... 19
Table 3.3Table of Ions of interest *(Gunn & Peterson, 1965, Morton, 2003)..... 21
Table 3.4 Selected summary of targets sightlines and observations of Quasar spectra and Lyman alpha systems of DLA systems with redshift..... 22
Table 3.5 Velocity dispersion and optical depth of absorber $zabs$ = 3.563 sightline 25
Table 3.6 Table for column density and metallicity of sightline 26
Table 3.7 Relative abundance of sightline..... 26
Table 3.8 Velocity dispersion and optical depth of absorber $zabs$ = 3.602 sightline 30
Table 3.9 Table for column density and metallicity of sightline 31
Table 3.10 Relative abundance of sightline..... 32
Table 3.11 Velocity dispersion and optical depth of absorber $zabs$ = 3.602 sightline 35
Table 3.12 Table for column density and metallicity of sightline 36
Table 3.13 Relative abundance of sightline..... 36
Table 3.14 Velocity dispersion and optical depth of absorber $zabs$ = 3.679 sightline 38
Table 3.15 Table for column density and metallicity of sightline 40
Table 3.16 Relative abundance of sightline..... 40
Table 3.17 Velocity dispersion and optical depth of absorber $zabs$ = 3.685 sightline 42
Table 3.18 Table for column density and metallicity of sightline 44
Table 3.19 Relative abundance of sightline..... 44
Table 3.20 Velocity dispersion and optical depth of absorber $zabs$ = 4.31 sightline 46
Table 3.21 Table for column density and metallicity of sightline 48
Table 3.22 Relative abundance of sightline..... 48
Table 4.1 Comparative representation of observed column density of selected sightlines 49
Table 4.2 Summary table of relative abundances and ratio of column density of C IV to Si IV of all selected absorber systems 50
Table A.1 The observed Sightlines with Coordinates, redshift of QSO and intervening gas-rich galaxies and column density 58

LIST OF FIGURES

Figure 1.1 Artesian diagram showing outflows, accreting, recycling in CGM (Tumlinson, Peeples, and Werk, 2017). 1
Figure 1.2 In galaxies, star formation cycles are depicted schematically, linking stars to chemical procession of the ISM (Som et al., 2015). 2
Figure 1.3 Observational properties of galaxies with reliability of theoretical models (Cimatti, Filippo Fraternali, & Nipoti, 2020). 6
Figure 3.1 Diagram illustrating the quasar absorption line method. This demonstrates the lines that are left on the quasar spectra as a result of material absorption along line of sight to quasar. (Tumlinson, Peeples, & Werk, 2017). 13
Figure 3.2 A diagram illustrating the quasar absorption line method. This shows the lines that are left on the quasar spectra as a result of material absorption along line of sight to quasar (Pettini 2003). 14
Figure 3.3 The equivalent width of an absorption line. Normalized continuum level in Ic = 1 is represented by horizontal dashed line. Solid red line represents the absorption line. The area of rectangular shaded region of unit height and the area beneath the line profile are equal. The comparable width of the absorption line defines the width of this rectangle (Som et al., 2015).. 18
Figure 3.4 Abundances by number of atoms of different elements are shown here on a logarithmic scale Solar abundance of different elements relative to H. Data of abundance are belongs to Asplund, Grevesse, Sauval, and Scott (2009). 20
Figure 3.5 a. Voigt Profile fit of Lyman-α for DLAs with $zabs$= 3.563 b. Radial velocity for system $zabs$ 23
Figure 3.6 Radial velocity vs Optical Depth and absorption fraction with reference to O I 1302.2, Si II1304, Si II 1527, C IV 1548 and Al II 1671 24
Figure 3.7 Gaussian fit for each element of $zabs$ 3.563, Wavelength (Å) vs flux (10^{-17}erg cm^{-2} s^{-1}Å^{-1}) 26
Figure 3.8 a. Voigt Profile fit of Lyman-α for DLAs with $zabs$= 3.602 b. Radial velocity for system $zabs$ 27
Figure 3.9 Radial velocity vs Optical Depth and absorption fraction with reference given elements 29
Figure 3.10 Gaussian fit for each element of $zabs$ 3.563, Wavelength (Å) vs flux (10^{-17}erg cm^{-2} s^{-1}Å^{-1}) 31
Figure 3.11 a. Voigt Profile fit of Lyman-α for DLAs with $zabs$= 3.611 b. Radial velocity for system $zabs$ 33
Figure 3.12 Radial velocity vs Optical Depth and absorption fraction with reference given elements 34
Figure 3.13 Gaussian fit for each element of $zabs$ 3.611, Wavelength (Å) vs flux (10^{-17}erg cm^{-2} s^{-1}Å^{-1}) 36
Figure 3.14 a. Voigt Profile fit of Lyman-α for DLAs with $zabs$= 3.679 b. Radial velocity for system $zabs$ 37
Figure 3.15 Radial velocity vs Optical Depth and absorption fraction with reference given elements 38
Figure 3.16 Gaussian fit for each element of $zabs$ 3.611, Wavelength (Å) vs flux (10^{-17}erg cm^{-2} s^{-1}Å^{-1}) 39

Figure 3.17 a. Voigt Profile fit of Lyman-α for DLAs with $zabs$= 3.679 b. Radial velocity for system $zabs$ 41
Figure 3.18 Radial velocity vs Optical Depth and absorption fraction with reference given elements 42
Figure 3.19 Gaussian fit for each element of $zabs$ 3.685, Wavelength (Å) vs flux (10^{-17}erg cm^{-2} s^{-1}Å^{-1}) 43
Figure 3.20 a. Voigt Profile fit of Lyman-α for DLAs with $zabs$= 4.31 b. Radial velocity for system $zabs$ 45
Figure 3.21 Radial velocity vs Optical Depth and absorption fraction with reference given elements 46
Figure 3.22 Gaussian fit for each element of $zabs$ 3.685, Wavelength (Å) vs flux (10^{-17}erg cm^{-2} s^{-1}Å^{-1}) 47

TABLE OF CONTENTS

DECLARATION ii

RECOMMENDATION iii

ACKNOWLEDGEMENTS iv

शोध सार v

ABSTRACT vi

LIST OF ACRONYMS AND ABBREVIATIONS vii

LIST OF SYMBOLS viii

LIST OF TABLES ix

LIST OF FIGURES x

CHAPTER 1 1

1. INTRODUCTION 1

1.1 INTRODUCTION 1

1.2 COMPOSITION OF THE ISM 2

1.2.1 FORMATION OF METAL ELEMENTS 3

1.3 THE PROCESS OF INTRODUCING HEAVY ELEMENTS INTO ISM 4

1.4 OBSERVATIONAL COSMOLOGY IN THE SIGNATURE OF SPECTRAL LINE 6

1.5 RATIONALE OF STUDY 7

1.6 OBJECTIVES OF STUDY 8

CHAPTER 2 9

2. REVIEW OF LITERATURE 9

CHAPTER 3 13

3. RESEARCH METHOD AND METHODOLOGY 13

3.1 QUASAR ABSORPTION LINE SYSTEMS 13

3.2 LYMAN ALPHA SYSTEM 15

3.3 DETERMINATION OF COLUMN DENSITIES 17

3.4 DETERMINATION OF ABUNDANCES 18

3.5 DATA SELECTION FROM SDSS AND DATA REDUCTIONS 20
3.6 ANALYSIS OF OBSERVED DATA 22

CHAPTER 4 49

4. RESULT AND DISCUSSION 49
Absorber at z = 3.563 along the sightline to J0811+3727 50
Absorber at z = 3.602 along the sightline to J1015+3921 51
Absorber at z =3.611 along the sightline to J0821+4022 51
Absorber at z = 3.679 along the sightline to J1305+0521 51
Absorber at z = 3.685 along the sightline to J1203+3411 51
Absorber at z = 4.31 along the sightline to J1050+4411 51

CHAPTER 5 52

5. CONCLUSIONS AND FUTURE WORK 52
5.1 CONCLUSIONS 52
5.2 FUTURE WORK 53

6. REFERENCES 54

APPENDIX A 58

7. OBSERVED SIGHTLINES 58

8. APPENDIX B 59

9. NULL GEODESICS IN FRW METRIC 59

CHAPTER 1

INTRODUCTION

1.1 INTRODUCTION

As the universe predominantly consists of neutral hydrogen, significance of gas takes parts in a fundamental role in formation and evolution of galaxies. Galaxy evolution and formation can be greatly supported by studying chemical properties of the interstellar medium (ISM) and provides valuable insights into this cosmic process of the continuous cycle of star formation relying on interstellar gas.

Galaxy formation involves complex interplay between star formation, metal enrichment, gas accretion, and feedback processes (Tumlinson et al. 2011). Knowledge of several key elements, including the time period when the first galaxies formed; morphologies and chemical contents, mechanisms and their evolution over cosmic time is significant for deciphering evolution and origins of galaxies in the universe (Maiolino & Mannucci 2019).

As galaxies evolve, they undergo continuous cycles of gas inflows and outflows. Gas inflows, primarily from the intergalactic medium, fuel star formation and contribute to galaxy growth. Outflows, driven by active galactic nuclei, supernova explosions, and stellar winds, metals and expel gas (elements heavier than hydrogen and helium) into the circumgalactic medium (CGM). These outflows regulate star formation by removing gas and enriching the surrounding environment with metals. The production of metals within galaxies occurs primarily through stellar nucleosynthesis, where elements are synthesized through ejected into ISM and nuclear fusion in stars through supernova explosions and stellar winds, which is shown in Figure 1.1.

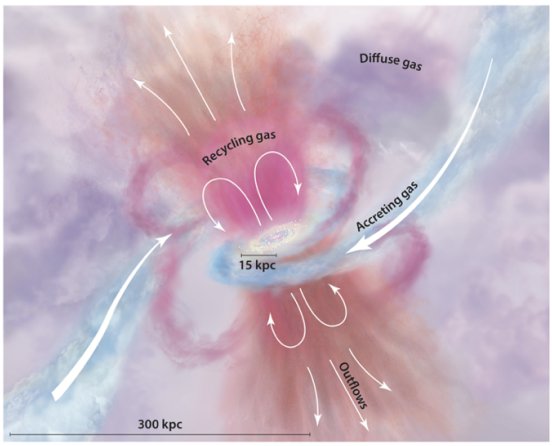

Figure 1.1 Artesian diagram showing outflows, accreting, recycling in CGM (Tumlinson, Peeples, and Werk, 2017).

Various elements generated during these activities are gradually liberated into the interstellar medium at different epochs, influenced by mixing mechanisms, ejection and productions. In turn, supply of interstellar gas to evolution of next generation of stars, perpetuating a cyclical process (see Figure 1.2). As a result, the properties of chemical composition of ISM offer crucial insights into its star formation history and accretion.

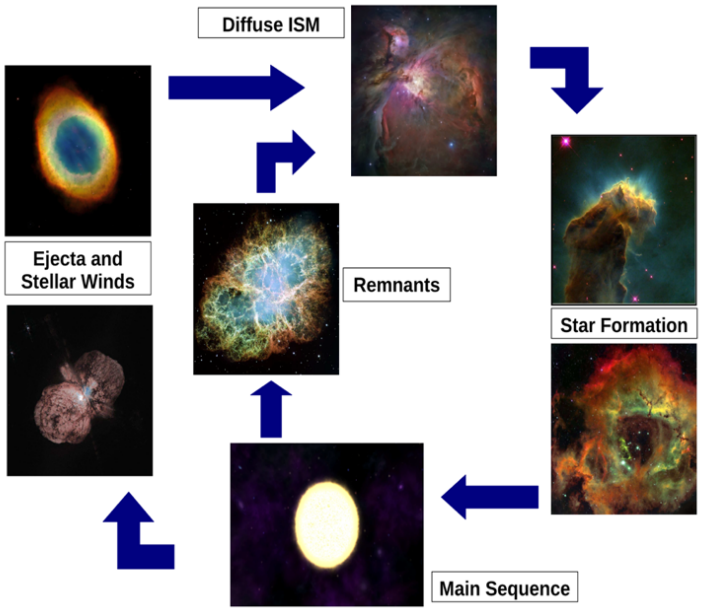

Figure 1.2 In galaxies, star formation cycles are depicted schematically, linking stars to chemical procession of the ISM (Som et al., 2015).

This chapter summarizes the physical structure of the ISM, physical mechanisms controlling photon-interstellar gas interactions follows observables.

1.2 COMPOSITION OF THE ISM

Space between the celestial bodies is called the Interstellar Medium. Effect of cosmic rays and photons, penetration of magnetic field and absorption of radiation by dust grains, presence of microwave background radiation etc. occurs within ISM. Generally, ISM contains mostly gas and dust (Som et al., 2015).

Gas

About 99% of the ISM is composed of gas, for which 75% is of Hydrogen mass and 25% is of Helium gas. Interstellar gas can also be divided into two forms: Hot ionized Hydrogen Cold atomic and molecular neutral Hydrogen.

Generally red color nebulae seen in sky are considered as the emission of visible light due to the ionization of gas caused by ultraviolet radiation released by newly formed stars. Also, radio waves are emitted when cold clouds of neutral hydrogen go to gravitational collapse.

Dust

Interstellar dust is simply composed of extremely small particles, nearly in the size of wavelength of blue light, having irregular size and are composed of Carbon, Silicates, iron and ice compounds. Dust can block light from extra-galactic and intergalactic sources.

Metal

In Astrophysics, heavier elements beside Hydrogen and Helium are called metal. The fundamental understanding of evolution of stars, galaxies and the whole universe cannot be complete without understanding the nature of gas and metallic elements. So, the presence of such metallic element can be the crucial link to know about the star formation and evolution history. This project work will be focused on the abundances of such metallic element of early environment.

1.2.1 FORMATION OF METAL ELEMENTS

Due to supernovae explosion and stellar winds, heavier elements are injected in ISM. Which determine the temperature of gas clouds and corresponding evolution. When temperature declined to 10^9 K after Big bang, stable hydrogen was formed and fusion of Hydrogen nuclei made helium and so trace amount of Lithium. But it is still very low temperature for another heavier element to form. Here are following processes which make heavier elements in ISM. According to Som et al. (2015), the following process play role for the metal element production.

Charged particle Fusion

The energy required to stabilize the star against its gravitational pull play's role to produce heavier elements up to Fe peak lines i.e., atomic number $Z \leq 30$. Production of such elements also rely on mass of stars. To illustrate; solar mass generally produces He and C. But star with 8 to 10 times solar mass is sufficient to produce Fe peak elements (Som et al., 2015).

Fe peak line elements have maximum binding energy. To balance the Coulomb repulsion between nuclei the binding energy of elements heavier than Fe peak line is insufficient because the heavier element is needed to form the more fusion reaction become endothermic and unsustainable (Som et al., 2015).

S-Process

Emission of neutrons during Fusion reaction is slower process than the β-particle decay rate. This neutron helps to form heavier element with $Z \geq 30$. The example of S-process is (Som et al., 2015).

$$^{13}_{6}\mathrm{C} + \alpha \rightarrow {}^{16}_{8}\mathrm{O} + \mathrm{n} - 0.91\ \mathrm{MeV}. \quad (1.1)$$

$$^{10}_{22}\mathrm{Ne} + \alpha \rightarrow {}^{25}_{12}\mathrm{Mg} + \mathrm{n} - 0.48\ \mathrm{MeV}. \quad (1.2)$$

R-Process

while supernovae explosion occurs, massive number of neutron rich isotopes decays to form most of the stable heavier elements due to accumulation of free neutron in electron capture interaction (Som et al., 2015).

$$\mathrm{p} + \mathrm{e} \rightarrow \mathrm{n} + \upsilon_e \quad (1.3)$$

1.3 THE PROCESS OF INTRODUCING HEAVY ELEMENTS INTO ISM

Supernova explosions and stellar winds plays crucial roles in enriching the interstellar medium (ISM) with heavier elements. Stellar winds arise from thermal pulsations during the final stages of intermediate-mass stars ($\lesssim 10\ M_{\odot}$), forming planetary nebulae that ultimately disperse into ISM. Because planetary nebulae are intermediate mass progenitors, lighter elements such as nitrogen (N), carbon (C), oxygen (O), and helium (He) are mostly added to the ISM by these star winds. On the other hand, supernova explosions contribute heavier elements into the ISM. Different types of supernovae yield distinct distributions of heavier elements. For instance, Type I supernovae, lacking hydrogen lines in their spectra, can be further categorized into Type Ia, Type Ib, and Type Ic based on varying absorption lines. Type Ia supernovae result from material accretion onto a white dwarf from a red giant, enriching mostly Fe-peak components in the ISM, including manganese (Mn), chromium (Cr), cobalt (Co), iron (Fe), and zinc (Zn). On the other hand, Type II supernovae, along with Types Ib and Ic, are large stars approach the end of their lives, their gravitational collapse produces core-collapse supernovae. Type II supernovae enhance

ISM with α-elements like oxygen (O), carbon (C), silicon (Si), magnesium (Mg), sulfur (S), argon (Ar), and calcium (Ca), in addition to Fe - peak elements.

Besides Gravitational pull, thermal energy, and chemical reaction the only reason stars like sun exists luminous is because of the nuclear reaction. Nuclear fusion changes light elements into heavier elements and it is key source of stellar energy. Also, this is key process for synthesizing heavier elements available in the universe. The abundances of elements we observe today result from nuclear processes occurring within stars. As part of galactic and stellar evolution, these processes not only alter element abundances but also impact the physical properties of stellar interiors, atmospheres, and the interstellar medium. Theory of Nucleosynthesis is mainly based upon the determination of the elemental abundances. This can be processed with the detailed study of light coming from our galaxy, external galaxies, and even from early universe. The division of stars are based on the chemical composition and metallicity as below:

Population I

This belongs to the most metal rich stars out of all three populations. These stars can be rooted in spiral arms of Milky Way galaxy. Whereas, sun belongs to this population. There are more metal rich stars than sun as well with metallicity of range $-1 \lesssim [Fe/H] \lesssim 0.3$ and known as metal rich starts (Cooke, Pettini, & Steidel, 2017).

Population II

This belongs to the older and less bright stars with abundance of little bit heavier elements than Helium as compared to population I stars. These stars can be found in bulge of milky way galaxy. Despite their low metallicity which is less than that of the Population I star they contain relatively abundances of alpha elements like O and N as compared to Fe with metallicity of range $-3 \lesssim [Fe/H] \lesssim -1$ and known as metal poor stars (Cooke, Pettini, & Steidel, 2017).

Population III

After the Big bang mostly gas contents Beryllium, trace amount of Lithium, Helium and Hydrogen were present. After cooling down sufficiently the very first stars were started to form which are called population III stars without any heavier elements. These stars were very massive and have easily undergone nucleosynthesis process and formed first elements up to Fe peak with metallicity of range $-10 \lesssim [Fe/H] \lesssim -3$ extremely metal poor stars (Cooke, Pettini, & Steidel, 2017).

1.4 OBSERVATIONAL COSMOLOGY IN THE SIGNATURE OF SPECTRAL LINE

Studying ISM within galaxies is essential for enhancing our comprehension of the evolution of cosmic chemicals. The data from observations made outside of the Milky Way's local neighborhood is particularly valuable for this purpose. Interstellar gas emits radiation across various wavelength bands, with intensities influenced by factors such as temperature, ionization state, density, and proximity to other energy sources. This emission can take scattered radiation, molecular lines (e.g., CO, NH_3), or form of recombination lines (e.g., Hα). Researchers study ISM features using emission spectra or imaging techniques. Nevertheless, because of the inverse square law, diffuse nature of emission, and expansion of Universe, studying ISM becomes constantly more challenging at greater distances. Even with 8-10 m class telescopes, it can be very challenging and expensive to observe photon from stellar component of high-redshift galaxies. Most high-redshift galaxies with reasonable observers have exceptionally shining, often due to hosting active galactic nuclei or being starburst galaxies. However, flux-limited investigations of high-redshift galaxies may induce biases toward rare, luminous, star-forming systems, and these systems do not always represent normal galaxies.

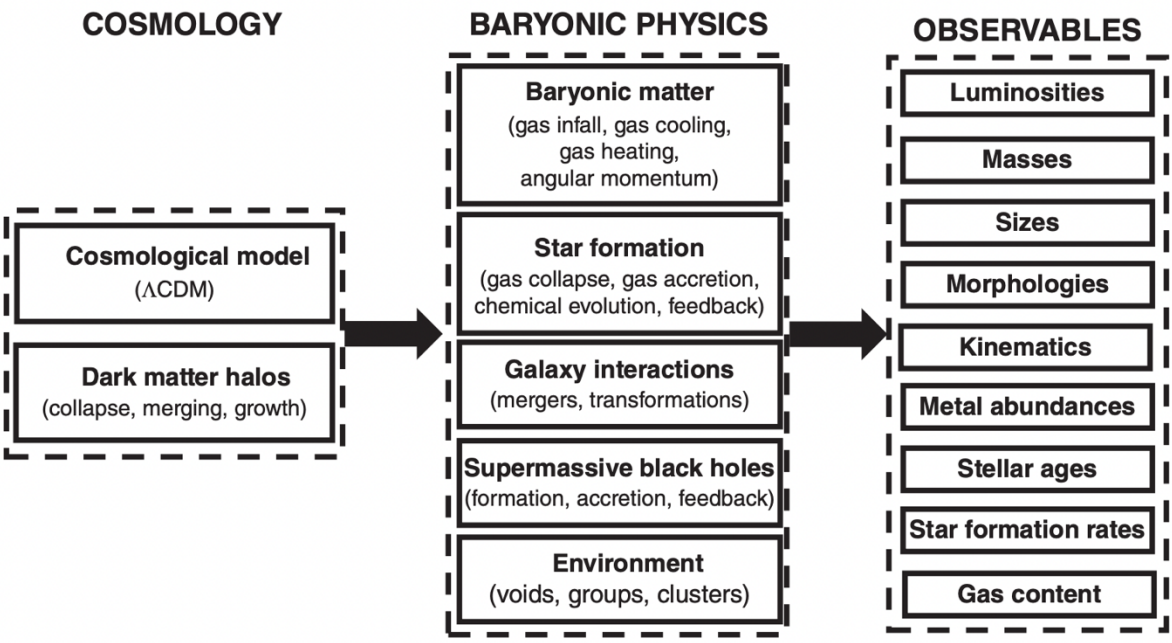

Figure 1.3 Observational properties of galaxies with reliability of theoretical models (Cimatti, Filippo Fraternali, & Nipoti, 2020).

However, studying galaxy formation and evolution involve both theoretical modeling and direct observation. Researchers study galaxies by observing them directly, collecting data such as images and spectra. From this data, they extract information about the physical and structural properties of galaxies, which is shown in Figure 1.3.

An alternative approach to understanding interstellar gas involves studying its absorption properties. Specifically, scientists analyze the absorption features imprinted on photons from background sources like quasars (detailed in Chapter 3). Unlike other methods, this absorption research is independent of brightness of foreground galaxies being examined and avoids biases associated with star forming galaxies. In this part, we introduce fundamental physical processes governing the interaction of photons with ISM, emphasizing observables relevant to absorption studies.

Understanding the physical processes and measurement techniques allows us to utilize absorption lines from interstellar gas effectively. These lines provide as an effective tool for investigating chemical enrichment state in galaxies across different time periods. Researchers frequently employ this technique to study the absorption line systems observed in distant quasars' spectra. Chapter 3 provides a foundation to these absorption line quasars. With help of this technique and apparent optical depth method, we can estimate metallicity and abundances, the measurable properties of intervening gas-rich galaxies as shown in Figure 1.3.

1.5 RATIONALE OF STUDY

Studying the lifecycle of metals and gas in a galaxy is important to understand the galaxy evolution and formation. Galaxies with high-redshift are very faint to study in emission-line technique, but can be observed in absorption. Background Quasars are generally used to probe the foreground galaxies. However, getting the high-resolution spectroscopic observation of quasars is very expensive, meanwhile, low resolution data from the all-sky survey such as SDSS are publicly available. This mini-research has planned to utilize the several spectra within redshift range of $3 \lesssim z_{abs} \lesssim 5$ from the SDSS survey for high-redshift galaxies to identify and study the kinematic and chemical properties of the gas-rich galaxies (Damped Lyman-alpha systems (DLAs)). As the measurements on the absorption lines produced by different elements in various ionization stages,

their column densities can be determined, which in turn, reveal information on chemical composition, ionization, and other physical properties of the absorbing gas. This research project will investigate an approach to robustly identify the absorption related to these absorbers.

1.6 OBJECTIVES OF STUDY

General Objective

- To identify and study the better understanding of galactic and interstellar chemical evolution of gas-rich quasar absorption-line systems behavior in the low-resolution spectra from SDSS survey with a wider range of high-redshift.

Specific Objectives

- To estimate the H I column densities and categorize the galaxies into DLAs and Sub-DLAs.
- To study the significance of determining the metallicity, relative abundance and gas kinematics from the perspective of low-resolution data.
- To distinguish strong vs weak absorption systems.
- To study photoionization, dust depletion in circumgalactic medium (CGM).

CHAPTER 2

REVIEW OF LITERATURE

As seen from Chapter 1, study of absorption signatures imprinted on spectra from background sources such as quasars is a powerful way to learn about interstellar gas in galaxies at high redshifts. The absorption lines give us plentiful information about the chemical enrichment of the CGM, and ISM. Specifically interesting absorption systems are the gas-rich galaxies in the intervening systems, where column density is $\log N_{H\,I} > 20.3$ cm^{-2} and $19.0\ cm^{-2} \leq \log N_{H\,I} \leq 20.3\ cm^{-2}$, respectively, for the DLAs and sub-DLAs. This chapter thoroughly provide the history of literatures that comprise of DLAs/sub-DLAs for studying their abundances and gas kinematics using higher resolution spectra.

Poudel, Kulkarni, Som, and Peroux (2021) performed various data analysis techniques, including measuring the metallicities, molecular gas fractions, and star formation rates of the observed galaxies. Authors also fit various models to the data to investigate the relationships between these properties and the galactic environment at high redshifts. The observed gas-rich galaxies at high redshifts have lower metallicities and higher molecular gas fractions compared to local galaxies, suggesting that they are in an early phase of chemical evolution. The authors discuss the implications of these findings for our understanding of galaxy formation and evolution in the early universe. The work demonstrated high-resolution systems of sub-DLAs within range of $2.173 < z_{abs} < 2.635$ and finds spread in metallicities. Which are ranges from -1.27 dex to +0.40 dex. The authors also put constraints on the electron density and determine cooling rate for sub-DLA with z = 2.173. And put forward idea of higher SFR density in those sub-DLAs than SFR density with DLAs with similar redshifts.

Maiolino and Mannucci (2019) researched the Cosmic Chemical Evolution of Galaxies in 2019. This study demonstrates the ability to analyze chemical abundances and metallicity on geometrical gradients can shed light on another internal phenomena like stellar migration, galactic fountains, and radial gas inflows as well as processes which governed assembly and growth of galaxies. The investigation of the chemical abundances in the galaxies are vast and intricate area of several unresolved issues with inconsistent findings.

Poudel et al. (2019) investigated abundances of DLA ($z_{abs} > 4.5$) and sub-DLA ($z_{abs} > 4.5$) along the line of sight, by using high-resolution data from the spectra of quasars that exhibit DLAs and

sub-DLAs were observed using different spectrographs. Specifically, the MIKE and MagE spectrographs on Magellan-South, as well as the X-Shooter spectrograph on the Very Large Telescope, were used to obtain these measurements. These systems were traced in absorption against bright background quasars at high redshifts 3.0 Through Voigt profile fitting, they calculated the column densities of H I and other elements found in the DLA and sub-DLA. The metallicities of the DLA and sub-DLA were calculated from the DLA via, which exhibits Ly-α emission from its host galaxy and has [C/O] ratio and [Si/O] ratio to confine nucleosynthesis models.

Cooke, Pettini, and Steidel (2017) explored metal-poor DLAs and provided understanding on chemical development in extremely metal-poor regime. To ascertain source of the metals in very metal-poor DLAs, they created abundance pattern for a typical very metal-poor DLA, compared to the model predictions of Population III and Population II nucleosynthesis. Findings suggested that most metal-poor DLAs were enhanced by generation of metal-free galaxies, because abundance data for a limited number of elements are available online; authors haven't ruled out the contribution for Population II stars.

Poudel et al. (2018) observed and studied the abundances of O, C, Si and Fe for high redshift (z_{abs}~5) galaxies which tries to constrain the early nucleosynthesis. Data from Very Large Telescope (VLT) and Keck telescope were used and with the help of undepleted element Oxygen, the corresponding metallicities and dust depletion were obtained. Also, the relative abundance including undepleted elements for the absorber with redshift $z_{abs} \geq 4.5$ are compared to lower z absorbers that helped to understand early chemical history of galaxies. Almost all of the column densities of Fe II, H I, Si II, C II, and O I were determined using Voigt profile fitting. This paper suggested that high redshift absorbers have low metallicity of [C/O] and [Si/O] ratios that supported chemical evolution models.

Morrison et al. (2016) conducted research on the element abundances of gas-rich galaxies at $z_{abs} = 5$, providing hints about the galaxies' early chemical richness. They investigated the chemistry and kinematics of a sub-DLA outflow that was enriched by early stars at $z_{abs} = 5$. At these high redshifts, they measured depleted or mildly undepleted elements like Oxygen in another DLAs and sub- DLAs. Physical differences between early-type and late-type galaxies are not thoroughly studied.

Frebel and Norris (2015) reviewed archaeologically evaluated the stellar and dwarf galaxies using method of chemical abundance for the different elements in extremely metal-poor stars, where authors emphasized carbon- normal and carbon-rich halo star populations. They presented an insightful idea on population III star progenitors with the events of the first metal enrichment. The near-field cosmology i.e., investigation of origins and evolution of universe was also investigated, where authors studied the association between the earliest stars and galaxies with the help of metal-poor stars that may be utilized to moderate their processes.

Becker, Bolton, and Lidz (2015) ascertained when and how the earliest galaxies re-ionized the IGM and the history of baryons, and analyzed the re-ionization with higher redshift galaxies from QSO absorption Lines. They discussed crucial role to the Ly-α Forest in determining the global ionizing emissivity budget and the strength of the ionizing ultraviolet backdrop, and they examined different ways in which absorption lines, near the reionization epoch, trace the relationship between galaxies and the intergalactic medium.

Khare (2013) provided a review of quasar absorption lines in his article. Since these items' discoveries, absorption lines have been suspected to exist. A single quasar's spectra may contain many absorption line systems, also known as absorption line groups, with each system having a unique redshift. While those with redshifts near to the quasar's are thought to have been created by material intrinsic to the quasar, the majority of these systems are thought to have been created by galactic or intergalactic clouds. Thus, these systems provide a sensitive probe to comprehend the quasar environment as well as the development of the Universe throughout the past 90% of its age.

Noterdaeme et al. (2012) studied SDSS-III DR9 to extract column densities of neutral H and metal ions along lines of sight of quasar. They also used statistical and computational methods to analyze the distribution of column densities and derive cosmological mass density of neutral gas. They determine cosmological mass density and column density distribution of neutral gas, derived from the absorption lines seen in the spectra of quasar. The column density distribution of neutral H in DLAs at redshift of 2.5 and characterize progression of neutral gas presence in DLAs of cosmological evolution at redshifts between 2 and 3.5. They found that the neutral gas density in DLAs decreases with increasing redshift. They derived H I column density distribution and

characterized neutral gas in DLAs at $2 < z_{abs} < 3.5$. The authors have found that the amount of neutral gas contained for star formation all over cosmic history can be used to confine the models of galaxy formation and evolution.

Asplund, Grevesse, Sauval, and Scott (2009) studied the present state of knowledge on the solar photo- spheric composition is assessed. The abundances of almost all elements are recalculated in this work, in part because of the use of a new, accurate, three-dimensional (3D), time-dependent hydrodynamical model of the solar atmosphere. The choice of spectral lines and the atomic input data are carefully taken into account.

Savage and Sembach (1991) studied the interstellar absorption lines with the help of apparent optical depth method. With the use of information from the International Ultraviolet Explorer (IUE) satellite, the conversion of the absorption line profile of any system into apparent optical depth and apparent column density per unit velocity is examined. Using Gaussian spread function, the empirical relationship between the true velocity-integrated column density of the absorption and the velocity-integrated column density were derived. Where the later one is inferred from the apparent column density profiles containing unresolved saturated structure were derived.

Most of the above research articles from past studied the metallicity of different selected ions of Carbon, Oxygen, Silicon, Aluminum, Zinc, Magnesium, Iron and others either for very low redshift absorption systems $z_{abs} \lesssim 1$ or very high redshift $z_{abs} \gtrsim 5$. Here we are going to study those intermediate high redshift range i.e., $3 \lesssim z_{abs} \lesssim 5$ along with column density $\log N_{H\,I} > 20.3$ cm^{-2} with apparent optical depth (AOD) method. We are conducting this research not on high resolution data but on low resolution data from SDSS. This research prioritized on relative abundances of [C/O] and [Si/O]. Also, to measure column density ratios of N (C IV)/N (Si IV) to constrain nucleosynthesis models, and measure the velocity dispersion to study the kinematics. We will achieve these by applying fitting the Gaussian using the spectra analysis tool called Linetools. We will also perform the Voigt profile fitting with the help of VoigtFit for determining H I column density.

CHAPTER 3

RESEARCH METHOD AND METHODOLOGY

Chapters 1 and 2 highlights the significance of studying absorption lines within spectra of bright background quasars. These lines serve a powerful tool for understanding interstellar gas within galaxies, particularly in the high redshifts. Among these systems of absorption line, quasar spectra have extensively utilized for purpose study. This chapter provides detailed explanation of the absorption systems.

The study of galaxy formation and evolution involves a complementary approach that combines theoretical modeling with direct observations of galaxies. By observing galaxies, we can collect data, including one-dimensional FITS spectra, which allows researcher to extract structural and physical properties. Analyzing ages along with metal abundances of stellar populations within a galaxy provides understandings into evolution of star formation along with heavy element enhancement over cosmic time. The most reliable results are obtained when individual stars within a galaxy can be observed.

3.1 QUASAR ABSORPTION LINE SYSTEMS

A quasar's sight line interacts with intervening gas at different locations within galaxies, including the IGM, CGM, and ISM. When observing the quasar's spectrum, astronomers detect absorption features from different chemical elements within these systems. The visual illustrates this process is shown in Figure 3.1.

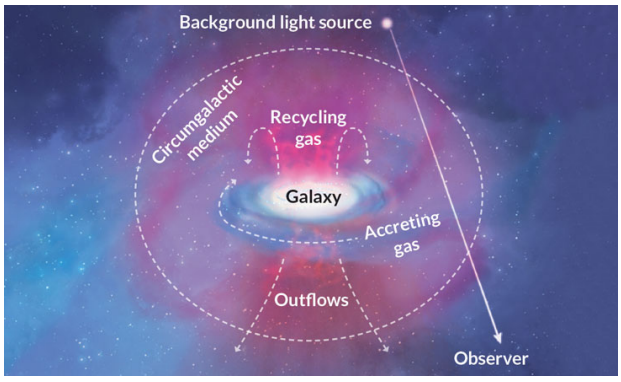

Figure 3.1 Diagram illustrating the quasar absorption line method. This demonstrates the lines that are left on the quasar spectra as a result of material absorption along line of sight to quasar. (Tumlinson, Peeples, & Werk, 2017).

In Figure 3.1, we see diagramatical illustration of line of sight toward quasar along with detected spectra. Broad peak in spectra corresponds to H emission originating from quasar itself. However, a strong H absorption at ~ 4700 Å is created by intervening galaxy (Asplund et al., 2009). To right of H-emission peak, we observe narrow absorption signatures due to metal absorption from the galaxy. To the left of the peak, there are additional features related to hydrogen absorption, which indicate different absorbers along the same line of sight. The absorption patterns observed in quasar spectra are dominated by hydrogen, the most abundant element in the universe. As most neutral hydrogen atoms in gas clouds are in the ground state, Lyman-series transitions specifically predominate in the characteristics generated by neutral hydrogen.

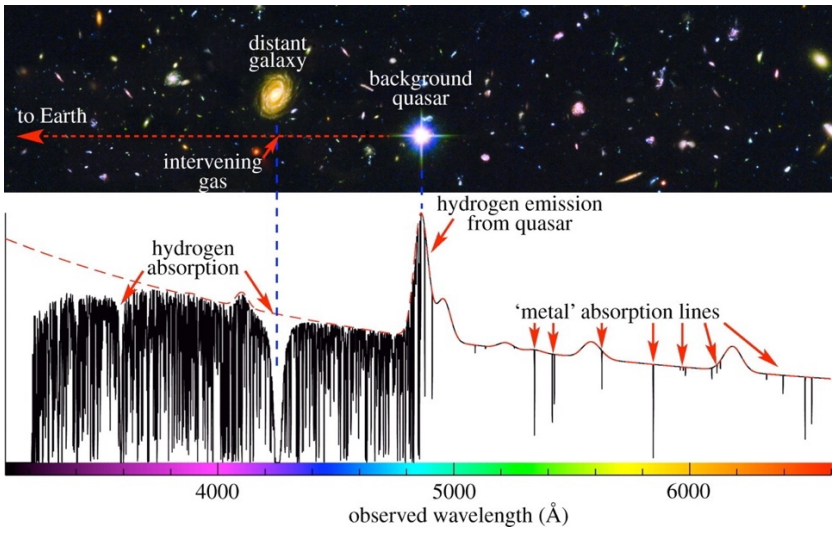

Figure 3.2 A diagram illustrating the quasar absorption line method. This shows the lines that are left on the quasar spectra as a result of material absorption along line of sight to quasar (Pettini 2003).

Technique utilizes to identify and investigate abundances of different chemical elements of foreground galaxies that absorbs the light from distant bright quasars by intervening gas clouds, providing valuable understandings into properties and evolution of intervening galaxies. Column densities to this material are high enough that a number of metal lines can also be detected in QSO spectra. Presence of these metal lines allows a more detailed characterization of the ionization state of the intervening material.

3.2 LYMAN ALPHA SYSTEM

High-redshift galaxies, formed in the early universe, are faint in emission due to their distance and young age, making them challenging to detect directly. However, Photons emitted by a distant quasar travel through the IGM/CGM. Along their path, they encounter intervening gas with varying densities and temperatures. Consequently, absorption features are imprinted on quasar's spectra. A QSO typically shines light across the whole electromagnetic spectrum peaking at UV wavelengths (in its rest frame). These photos can be absorbed by intervening gas located between the QSO and us. This absorption line technique offers a powerful means to study high-redshift galaxies.

Depend on the amount of H I in clouds of intervening gas to line of sights are classified as follows (Péroux et al. 2003, Prochaska et al. 2003a, 2003b, Kulkarni et al. 2005, Wolfe et al. 2005):

Table 3.1 Classification of Ly-α system based on column density (Péroux et al. 2003)

	Lyman-α System	$\log N_{H\,I}$	Location
1	Lyman-α forest	$\log N_{H\,I} < 17.2$	Filaments/Voids
2	Lyman Limit System (LLS)	$17.2 \leq \log N_{H\,I} \leq 19.0$	CGM/Filaments
3	Sub-Damped Lyman-α (sub-DLA)	$19.0 \leq \log N_{H\,I} \leq 20.3$	CGM/Galaxies
4	Damped Lyman-α (DLA)	$\log N_{H\,I} > 20.3$	Galaxies

3.3 APPARENT OPTICAL DEPTH (AOD) METHOD

The AOD method is the technique used to examine interstellar absorption lines. It entails converting observed absorption-line profiles into profiles of the column density (represented by N_u) and apparent optical depth (denoted as $\tau_a(\lambda)$).

The AOD method involves converting absorption-line information straightly into format which allows for scientific explanations of physical conditions within interstellar intervening medium based on velocity with help of spectra analysis tool called Linetools and Voigt profile fitting program VoigtFit.

Considering a point source of radiation traveling through the medium adds lights from other sources to beam. If medium is accountable for absorption, emission and scattering of lights (radiation) from the beam. Radiative transfer equation describes the following differential equation

can be used to describe how the beam intensity changes throughout the path length ds in the presence of absorbing and emitting matter:

$$\frac{dI_\lambda}{ds} = j_\lambda - \alpha_\lambda I_\lambda \tag{3.1}$$

Here, j_λ is emission coefficient, α_λ is absorption coefficient and I_λ is specific intensity. For simple case without emission i.e., $j_\lambda = 0$;

$$\frac{dI_\lambda}{ds} = -\alpha_\lambda I_\lambda \tag{3.2}$$

Integration from point 0 (background source) to s yields

$$\int_{I_o}^{I} \frac{dI_\lambda}{I_\lambda} = \int_0^s -\alpha_\lambda ds$$

$$\ln\left(\frac{I}{I_0}\right) = \int_0^s -\alpha_\lambda ds$$

$$I = I_0 e^{\int_0^s -\alpha_\lambda ds}$$

$$I = I_0 e^{-\tau_\lambda} \tag{3.3}$$

Here τ_λ is the optical depth and $\tau_\lambda = -\int_0^s \alpha_\lambda ds$, therefore the optical depth is an important parameter in radiative transfer because it determines the amount of radiation that is absorbed or scattered by an intervening medium. It is function of wavelength λ appears in spectra of an intervening medium. Here I_0 and I are the intensities without and with the absorption, respectively.

When absorption is documented with the instrument having a finite resolution. Which is defined by the instrumental spectral spread function, $\phi_\lambda(\Delta\lambda)$ the recorded spectrum is a convolution of the intrinsic spectrum and the spread function (Savage & Sembach, 1991)

$$I_{obs} = I_0 e^{-\tau_\lambda \otimes \phi_\lambda(\Delta\lambda)} \tag{3.4}$$

we define two kinds of optical depth,

$$\tau_\lambda = \ln\left(\frac{I}{I_0}\right) \tag{3.5}$$

And,

$$\tau_a(\lambda) = \ln\left(\frac{I}{I_0}\right) \tag{3.6}$$

The optical depth, τ_λ, obtained from equation is the true optical depth as determined from the true line profile. The optical depth, $\tau_a(\lambda)$, obtained from equation is hereafter referred to as the apparent optical depth (AOD). The apparent optical depth is an instrumentally version of the true optical depth.

The optical depth measures the thickness of the intervening medium, since $\tau_\lambda \ll 1$, optically thin (object is transparent) medium, $\tau_\lambda \gg 1$ optically thick (light of background objects is extinguished) medium. The AOD method used for deriving column densities from absorption-line measurements by integration of observed optical depth profile followed by next session below.

3.3 DETERMINATION OF COLUMN DENSITIES

Column densities were determined by fitting the normalized absorption profiles using Voigt profile fitting program VoigtFit for H I column density. Number of molecules per unit area in the line of sight is called column density and the Formula for column density is (Som et al., 2015)

$$N_u = \int n_u ds \tag{3.6}$$

the column density as the number of molecules n_u in energy level u integrated over the path length ds. From measurements on the absorption lines produced by different molecules or elements in various ionization stages, their column densities can be determined, which in turn, reveal information on chemical composition, ionization, and other physical properties of the absorbing gas. For measuring the depth of absorption feature of selected data will be calculated with equivalent width (W), which is define as (Som et al., 2015)

$$W = \int_0^\infty \frac{I_c - I_\lambda}{I_c} d\lambda = \int_0^\infty (1 - e^{-\tau_\lambda}) d\lambda \tag{3.7}$$

here $I_\lambda$represents the intensity within the absorption line, while I_c corresponds to the intensity of the continuum. The continuum intensity refers to the background spectrum around the absorption line (Som, 2014). Furthermore, τ_λ represents optical depth measurements on the absorption lines resulting from distinct elements or molecules at different phases of ionization. The equivalent width of a continuum normalized spectrum, $I_c = 1$, can be conceptualized is the same width as the

bound of the spectral line in a rectangular box with unit height and area. Well description of this idea in Figure 3.3.

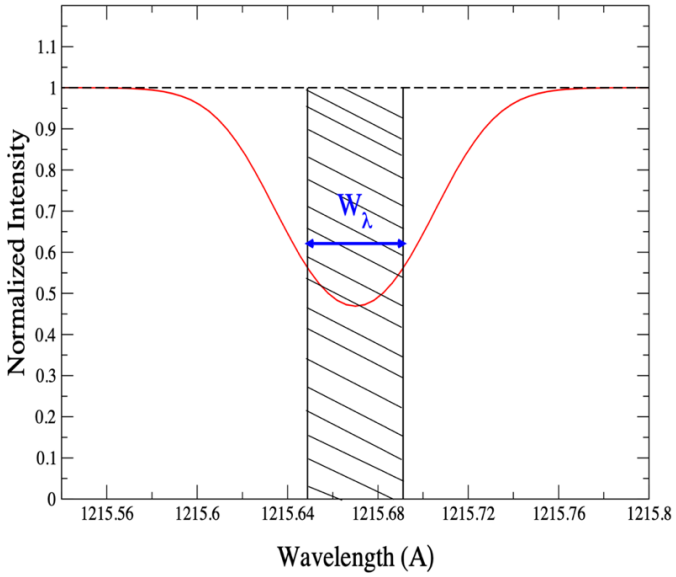

Figure 3.3 The equivalent width of an absorption line. Normalized continuum level in $I_c = 1$ is represented by horizontal dashed line. Solid red line represents the absorption line. The area of rectangular shaded region of unit height and the area beneath the line profile are equal. The comparable width of the absorption line defines the width of this rectangle (Som et al., 2015).

Because of Hubble tension, observed equivalent width (represented by W_{obs}) of an absorption line from a cloud at redshift z_{abs} (intervening gas-rich galaxies) is expanded by the factor $(1 + z_{abs})$ compared to the equivalent width at the rest frame (W_{rest}) of the absorber.

$$W_{obs} = W_{rest}(1 + z_{abs}) \tag{3.8}$$

3.4 DETERMINATION OF ABUNDANCES

The abundance of metals with respect to hydrogen in the stellar bodies is known as metallicity. For Metallicity

$$[X/H] = \log(N_X/N_H) - \log(X/H)_{\odot} \tag{3.9}$$

Here, N_X, N_H are column densities of elements X, Hydrogen (Som et al., 2015). The evolution of ISM can be understood with the evolution of metal elements. N_X, N_H are column densities of elements will be determined from above session of column densities. For Relative abundances

$$[X/Y] = \log(N_X/N_Y) - \log(X/Y)_\odot \quad (3.10)$$

Here, N_X, N_Y are column densities of elements X, Y. Therefore, abundance of X relative to Y and $\log(X/Y)_\odot$ is solar system abundance ratio between X and Y. The solar system abundances are determined from measurements of Sun's photosphere. Solar abundances of selected elements commonly observed in ISM and purpose for this project are given in Table 3.2. The solar abundance pattern plot is shown in Figure 3.3. Abundance data aquired for this research follow from Asplund et al. (2009).

Table 3.2 Element Composition of solar photosphere elements (Asplund et al. 2009)

Atomic Number (Z)	Element	Solar Abundance $(X)_\odot$
1	H	12
6	C	8.43
8	O	8.69
12	Mg	7.60
13	Al	6.45
14	Si	7.51
16	S	7.12
26	Fe	7.50

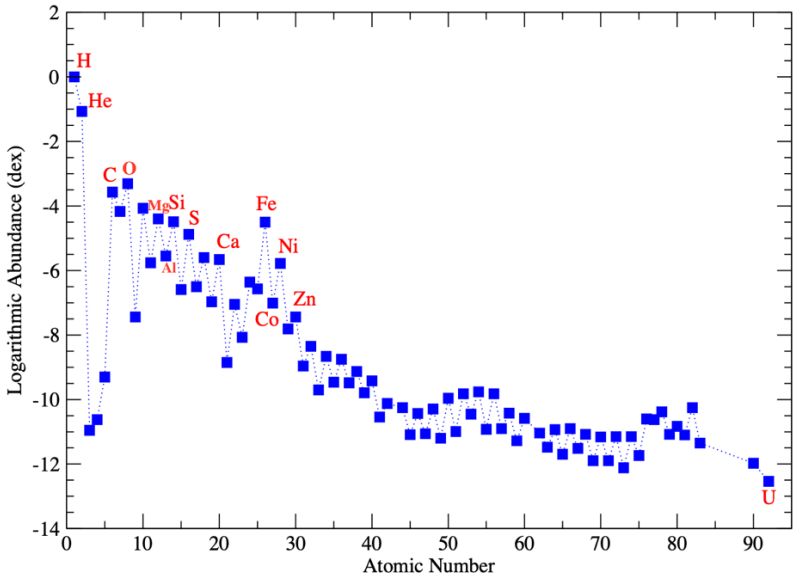

Figure 3.4 Abundances by number of atoms of different elements are shown here on a logarithmic scale Solar abundance of different elements relative to H. Data of abundance are belongs to Asplund, Grevesse, Sauval, and Scott (2009).

Understanding measurement and physical processes methods mentioned earlier, absorption line originating from interstellar gas serve as valuable tool for investigating chemical enrichment status of galaxies across different time periods. Researchers frequently employ this technique to examine the absorption line systems found in distant quasars' spectra.

3.5 DATA SELECTION FROM SDSS AND DATA REDUCTIONS

With the motivation of quasar absorption systems for better understanding the galactic chemical evolution, the data of quasar spectra will be chosen from VizieR Online Data Catalog with help of Noterdaeme et al. (2012) catalogue table J/A+A/547/L1, the corresponding individual observational ID's FITS spectra are downloaded from SDSS Data Release (DR)16. The spectra measures with SDSS have the wavelength coverage of 3,650 - 10,400 Å with exposure 54 sec ("Getting Started with the Optical Data | SDSS," (2024)), while the absorber system i.e., intervening system have redshift range of z_{abs} 1.951- 5.343 also the background QSO with redshift range of z_{qso} 2.01 – 5.605. Then corresponding atom in the ISM and CGM in the intervening gas rich galaxies are calculated with the help of cosmological redshift (Appendix B) i.e., Equation

B.13 is presented in the Table 3.3. The sightlines are selected and downloaded from the SDSS are within the wavelength coverage of SDSS of corresponding rest wavelength and oscillator strength of atoms from the Table 3.3 i.e., $3 \lesssim z_{abs} \lesssim 5$.

The selected Atoms/Ions have their corresponding transition levels such as I for the neutral atom, II for the singly ionized and IV for the triply ionized. Here in the Table 3.3, there are H I, O I and Mg I belonged to first transition, C II, S II, Si II, Fe II, Al II and Mg II are belonged to second transition and finally Si IV and C IV are belonged to triple transition.

Table 3.3Table of Ions of interest *(Gunn & Peterson, 1965, Morton, 2003)

Atom/Ion	Rest Wavelength* (Å)	Oscillator Strength*	Observed Wavelength (Å) respect to z_{abs} with compare to SDSS
H I	1215.6701	0.416400	3588.416 – 7713.088
S II	1253.811	0.0109	3700.554 – 7954.122
Si II	1260.4221	1.180	3719.440 – 7994.717
O I	1302.1685	0.048000	3842.792 – 8258.586
Si II	1304.3702	0.0863	3849.284 – 8273.809
C II	1334.5323	0.127800	3938.109 – 8461.562
Si IV	1393.76018	0.513	4113.694 – 8842.142
Si IV	1402.77291	0.254	4140.253 – 8899.229
Si II	1526.70698	0.13300	4506.177 – 9685.761
C IV	1548.2049	0.189900	4568.148 – 9818.964
C IV	1550.77845	0.094750	4577.001 – 9837.993
Fe II	1608.45085	0.0577	4745.208 – 10199.544
Al II	1670.7886	1.740	4931.121 – 10599.153
Mg II	2796.3553	0.6155	8250.996 – 17735.027
Mg II	2803.5324	0.3058	8271.653 – 17779.429
Mg I	2852.9634198	1.83	8416.352 – 18090.236

For this project, the wide range of red shift will select from VizieR Online Data Catalog with Damped Lyman-alpha absorption systems (DLAs) with neutral hydrogen column densities of $\log N_{HI} \gtrsim 20.3$ and Sub-Damped Lyman-alpha absorption systems (sub-DLAs) with $19.0 \lesssim \log N_{HI} < 20.3$ having the highest N_{HI} of quasars absorbers.

The catalogue containing columns of H I 1216 Å, C II 1334.5 Å, Si II 1527 Å, Fe II 1608 Å, Al II 1671 Å, Mg II 2796 Å, Mg II 2803 Å and Mg I 2852 Å along with 3 σ corresponding errors will be selected with criteria ions S II 1254 Å, O I 1302.2 Å, Si II 1304.4 Å, Si IV 1394 Å,1403 Å, C IV 1548 Å, 1551 Å within redshift range $3 \lesssim z_{abs} \lesssim 5$, having H I 1216 Å at log $N_{HI} \gtrsim 20.3$ and continuum to noise ration of 10.

3.6 ANALYSIS OF OBSERVED DATA

Column densities, velocity profile and optical depth of each FITS sightlines was calculated by applying a fit to the normalized absorption profiles with profile-fitting technique with Voigt profile fitting program VoigtFit and Linetools. Multiple components, each specific to the system, were used in the fits to the metal line absorption profiles seen in our data.

We are able to find only 6 relatively proper system among the 42 sightlines from table A.1 Appendix A with good absorption features and abundances detection. System which has low detection level than 3 are also discarded. Also, no proper absorption feature. The following table is the total 6 sightlines with redshift $3 \lesssim z_{abs} \lesssim 5$ and followed with discussion of individual absorber sightline;

Table 3.4 Selected summary of targets sightlines and observations of Quasar spectra and Lyman alpha systems of DLA systems with redshift

S.N.	QSO name	RA (J2000)	DEC (J2000)	z_{qso}	z_{abs}	log $N_{H\,I}$ (cm^{-2})
1.	J0811+3727	081132.2100	+372755.440	3.828	3.563	20.66
2.	J1015+3921	101526.3300	+392107.200	3.605	3.602	20.69
3.	J0821+4022	082159.5900	+402236.480	3.77	3.611	20.53
4.	J1305+0521	130502.2800	+052151.120	4.076	3.679	21.17
5.	J1203+3411	120359.0700	+341114.290	3.756	3.685	20.92
6.	J1050+4411	105049.2800	+441144.880	4.31	4.31	20.35

Absorber at z_{abs} = 3.563 along the sightline to J0811+3727

The absorber system z_{abs} of sightline towards the J0811+3727 is selected to study physical and chemical properties by using ions mentioned in Table 3.3. This is the lowest redshift in our selection list.

The Figure 3.5 a and b are the Voigt profile fitting program VoigtFit of the absorber system in order to determine column density of neutral Hydrogen (H I 1216). The profile is fitted with the column density 20.1 $\pm$ 0.2 dex, which is considered as sub-DLA according to Table 3.1.

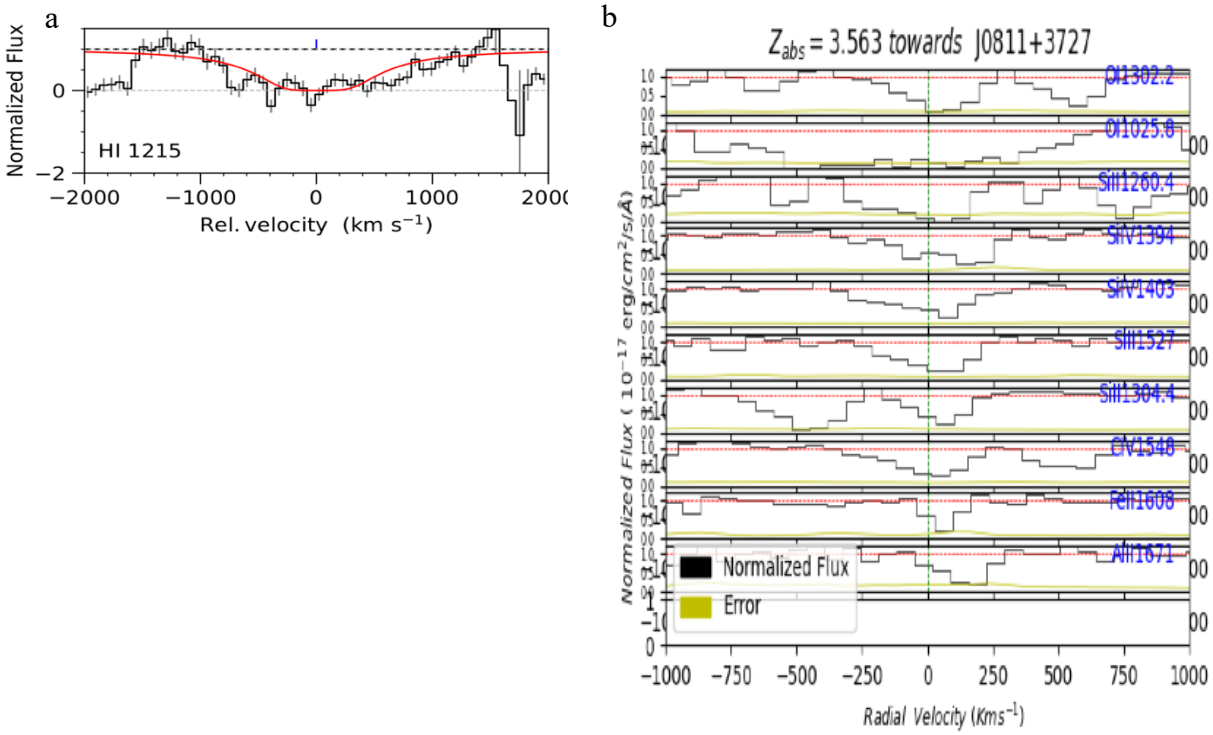

Figure 3.5 a. Voigt Profile fit of Lyman-α for DLAs with z_{abs}= 3.563 b. Radial velocity for system z_{abs}

Now from the study of the all the ions in the absorber's sightline, first we normalized flux and check if there are any unfit ions in order to sorted out from the well fitted ions with Linetools. From the Figure 3.8 b is the fitted plot for ions O I 1302.2, O I 1025.4, Si II 1260.4, Si IV 1394, Si IV 1403, Si II 1527, Si II 1304.4, C IV 1548, Fe II 1608 and Al II 1671 found in the system z_{abs} = 3.55. As O I 1025.8, Si II 1260.4, Si IV 1394, Si IV 1403 and Fe II 1608 is taking unusual area this ion will be neglected for further study. Remaining 5 ions are analyzed as below Figure 7

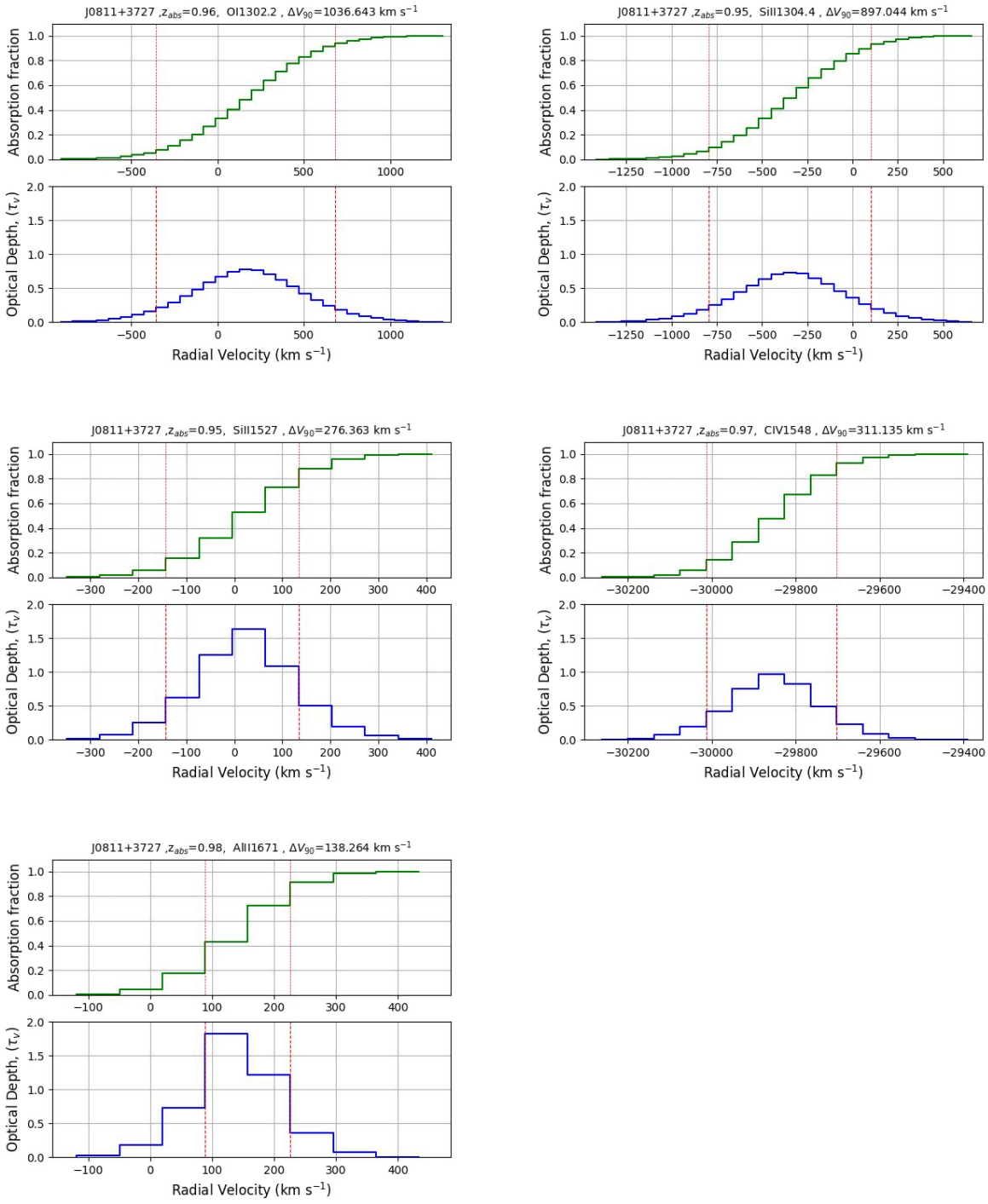

Figure 3.6 Radial velocity vs Optical Depth and absorption fraction with reference to O I 1302.2, Si II1304, Si II 1527, C IV 1548 and Al II 1671

Optical depth and velocity width of selected 5 ions O I 1302.2, Si II 1304.4, Si II 1527, C IV 1548 and Al II 1671 are studied and the values obtained are presented in Table 3.5 below. The observed sightline suggested it is optically thick sub-DLA system.

Table 3.5 Velocity dispersion and optical depth of absorber z_{abs} = 3.563 sightline

S.N.	Element	Velocity Width (km/s)	Optical Depth
1.	O I 1302.2	1036.6	0.8
2.	Si II 1304.4	897.1	0.7
3.	Si II 1527	276.4	1.6
4.	C IV 1548	311.1	0.9
5.	Al II 1671	138.3	1.8

The 1-dimensional spectra absorption feature of sightline was studied and estimated the column density with help of Linetools, the calculation was done within $\pm$ 0.2 dex presented in the figure 3.6.

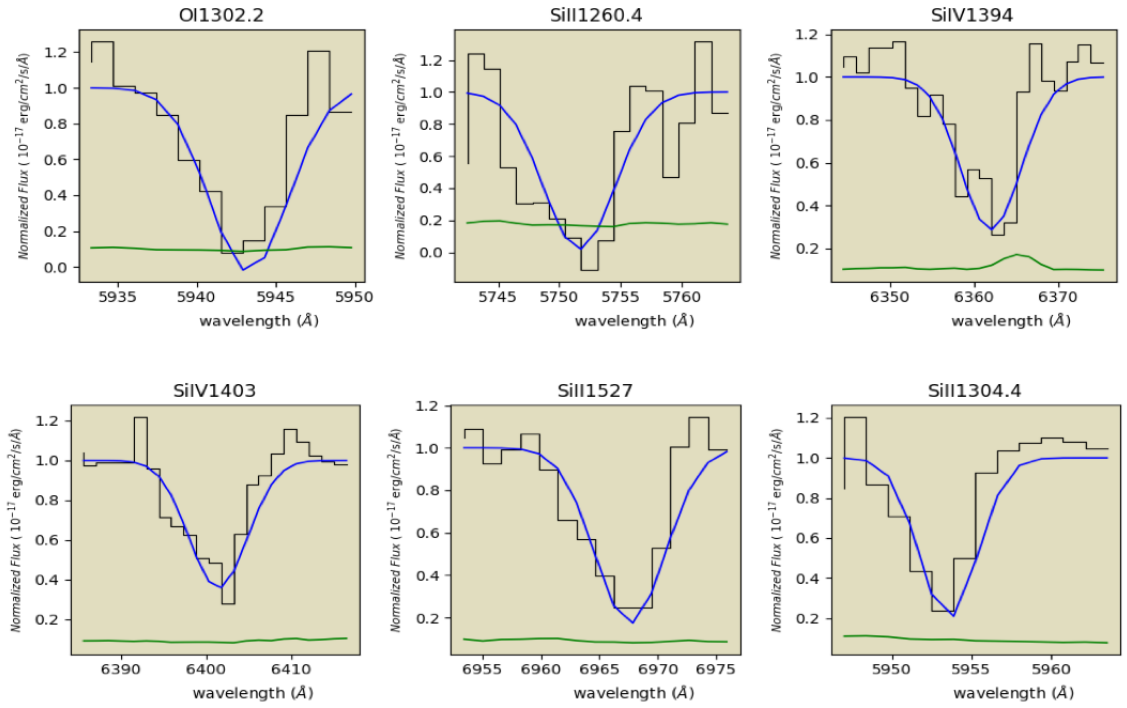

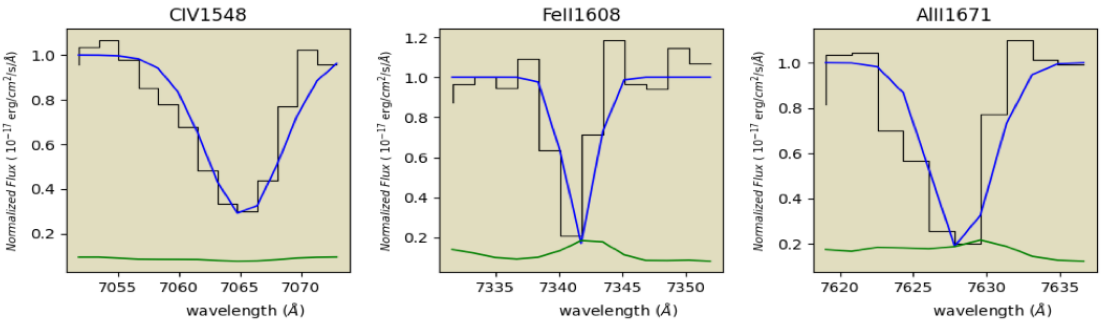

Figure 3.7 Gaussian fit for each element of z_{abs} 3.563, Wavelength (Å) vs flux (10^{-17}erg cm^{-2} s^{-1}Å^{-1})

The metallicity and relative abundances are estimated are presented in Table 3.6 and 3.7.

Table 3.6 Table for column density and metallicity of sightline

S.N.	Element [X]	W_X (Å)	log N_X (cm^{-2})	Metallicity [X/H]
1.	O I 1302.2	1.14	15.5	-1.29
2.	Si II 1260.4	1.71	14.36	-1.25
3.	Si II 1304.4	0.66	14.93	-0.68
4.	Si IV 1394	1.13	14.29	-1.32
5.	Si IV 1403	1.03	14.51	-1.10
6.	Si II 1527	1.22	14.87	-0.74
7.	C IV 1548	1.25	14.66	-1.87
8.	Fe II 1608	0.58	14.85	-0.75
9.	Al II 1671	0.98	13.59	-0.96

Table 3.7 Relative abundance of sightline

S.N.	Relative Abundance $\left[\frac{X}{Y}\right]$
1.	$\left[\frac{\text{Fe II}}{\text{O I}}\right] = 0.54$
2.	$\left[\frac{\text{Si II}}{\text{O I}}\right] = 0.04$

Absorber at z_{abs}= 3.602 along the sightline to J1015+3921

The absorber system z_{abs} of sightline towards the J1015+3921 is selected to study the chemical and physical properties by using the ions mentioned in the Table 3.3. This is the lowest redshift in our selection list.

The Figures 3.8 a and b are the Voigt profile fitting program VoigtFit of the absorber system in order to determine the column density of the neutral Hydrogen (H I 1216). The profile is fitted with the column density 20.25 $\pm$ 0.2 dex, which is considered as sub-DLA according to Table 3.1.

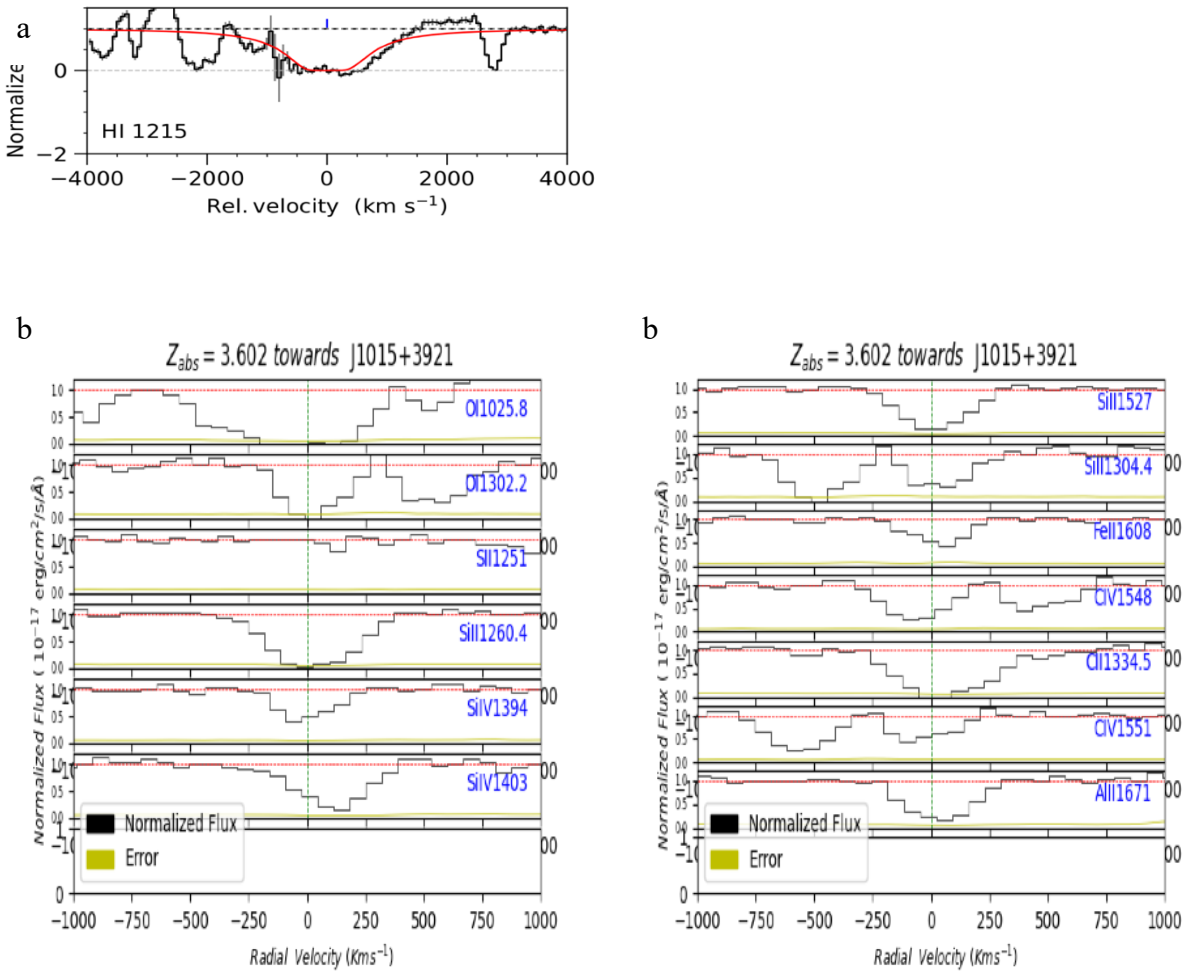

Figure 3.8 a. Voigt Profile fit of Lyman-α for DLAs with z_{abs}= 3.602 b. Radial velocity for system z_{abs}

Now from the study of the all the ions in the absorber's sightline, first we normalized flux and check if there are any unfit ions in order to sorted out from the well fitted ions with Linetools. From the Figure 3.8 b is the fitted plot for ions O I 1302.2, Si II 1260.4, Si IV 1394, Si IV 1403, Si II 1527, Si II 1304.4, C IV 1548, C II 1334.5 and Al II 1671 are detected in the system $z_{abs} = 3.602$. As C IV 1551 and Fe II 1608 is taking unusual area this ion will be neglected for further study. Remaining 9 ions are analyzed as below Figure 3.9.

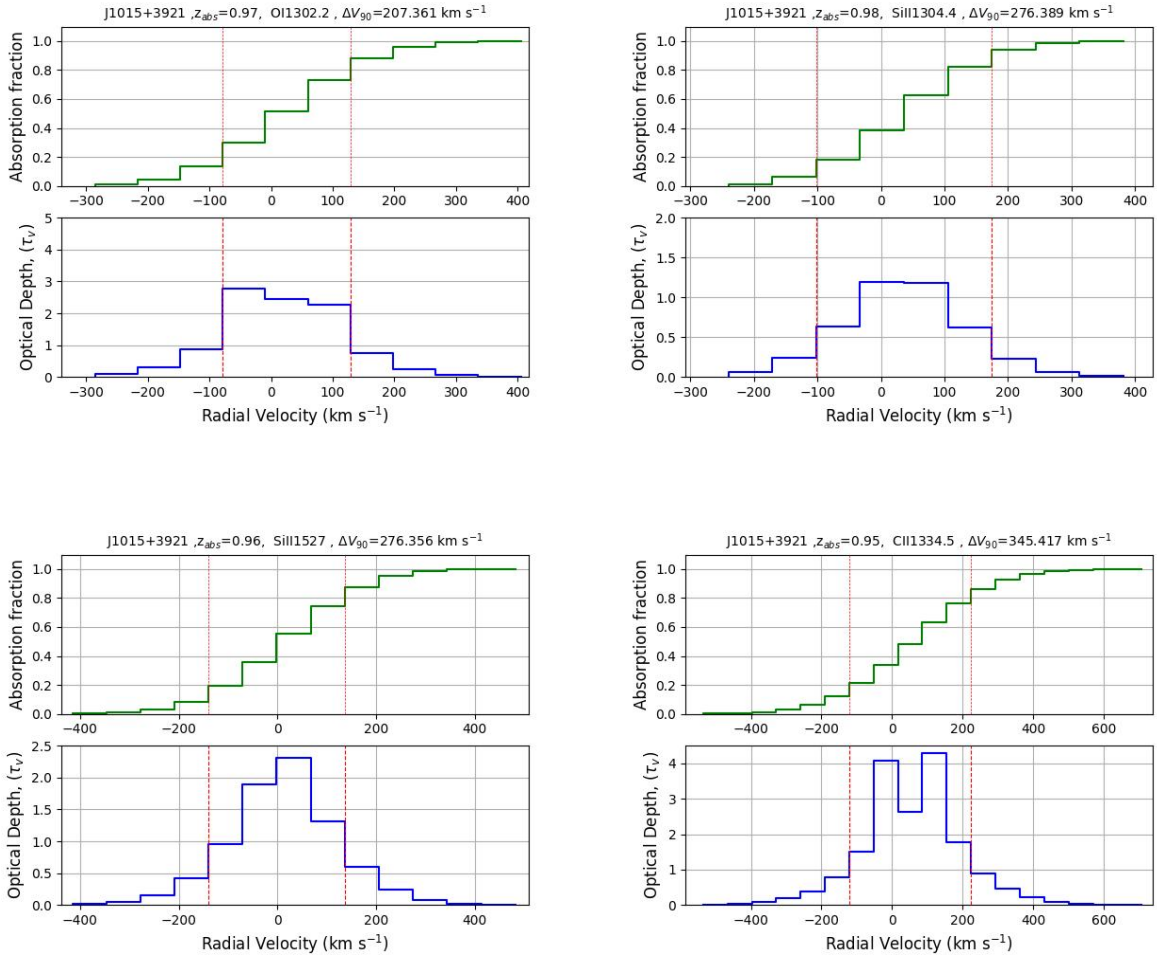

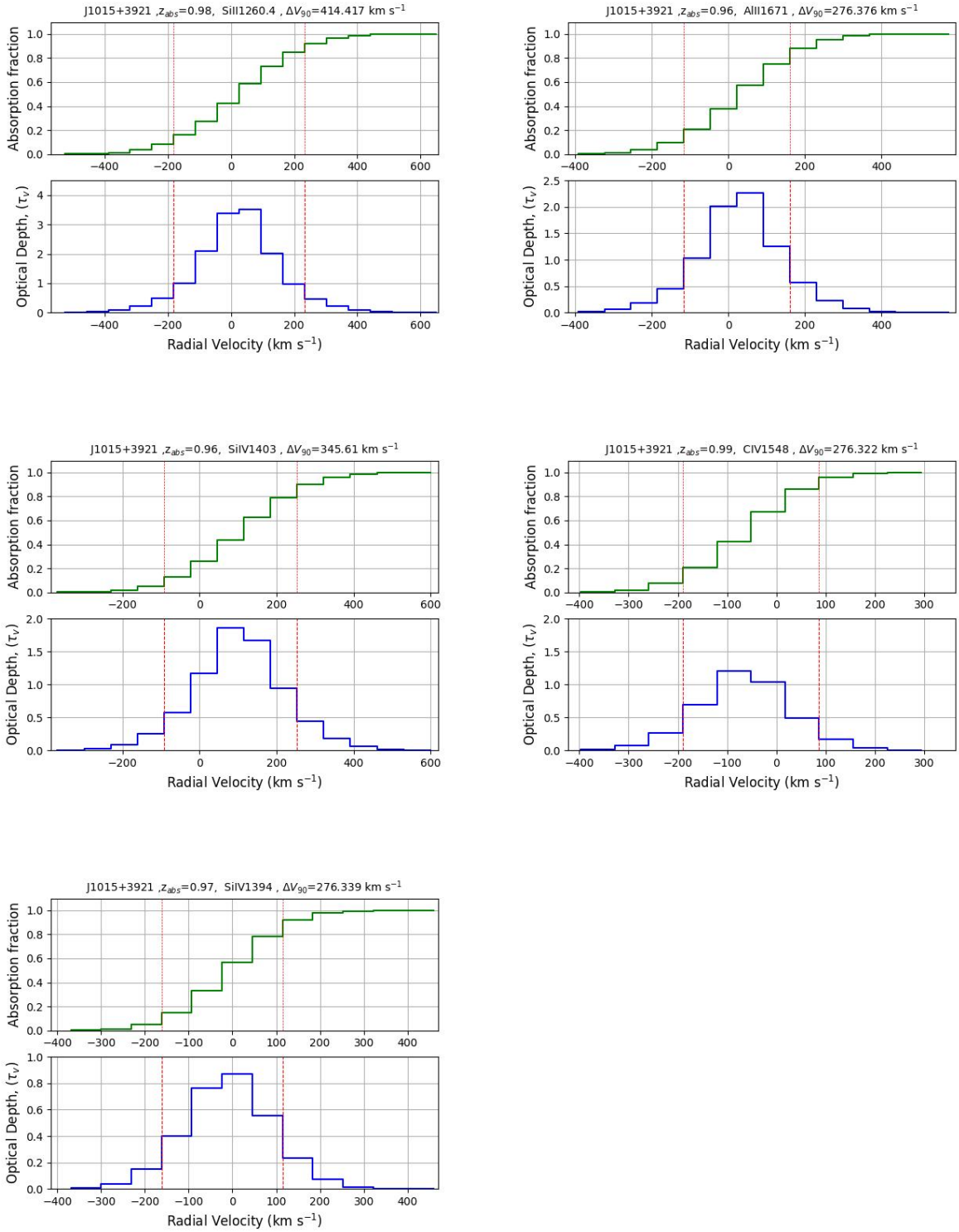

Figure 3.9 Radial velocity vs Optical Depth and absorption fraction with reference given elements

Optical depth and velocity width of selected 9 ions O I 1302.2, Si II 1260.4, Si IV 1394, Si IV 1403, Si II 1527, Si II 1304.4, C IV 1548, C II 1334.5 and Al II 1671 are studied and the values obtained are presented in Table 3.5 below. The observed sightline suggested it is optically thick sub-DLA system.

Table 3.8 Velocity dispersion and optical depth of absorber z_{abs} = 3.602 sightline

S.N.	Element	Velocity Width (km/s)	Optical Depth
1.	O I 1302.2	207.4	2.8
2.	Si II 1260.4	414.4	3.5
3.	Si II 1304.4	276.4	1.2
4.	C II 1334.5	345.4	4.3
5.	Si IV 1394	276.3	0.9
6.	Si IV 1403	345.6	1.9
7.	Si II 1527	276.4	2.3
8.	C IV 1548	276.3	1.2
9.	Al II 1671	276.4	2.3

The 1-dimensional spectra absorption feature of sightline was studied and estimated the column density with help of Linetools, the calculation was done within $\pm$ 0.2 dex presented in the Figure 3.10.

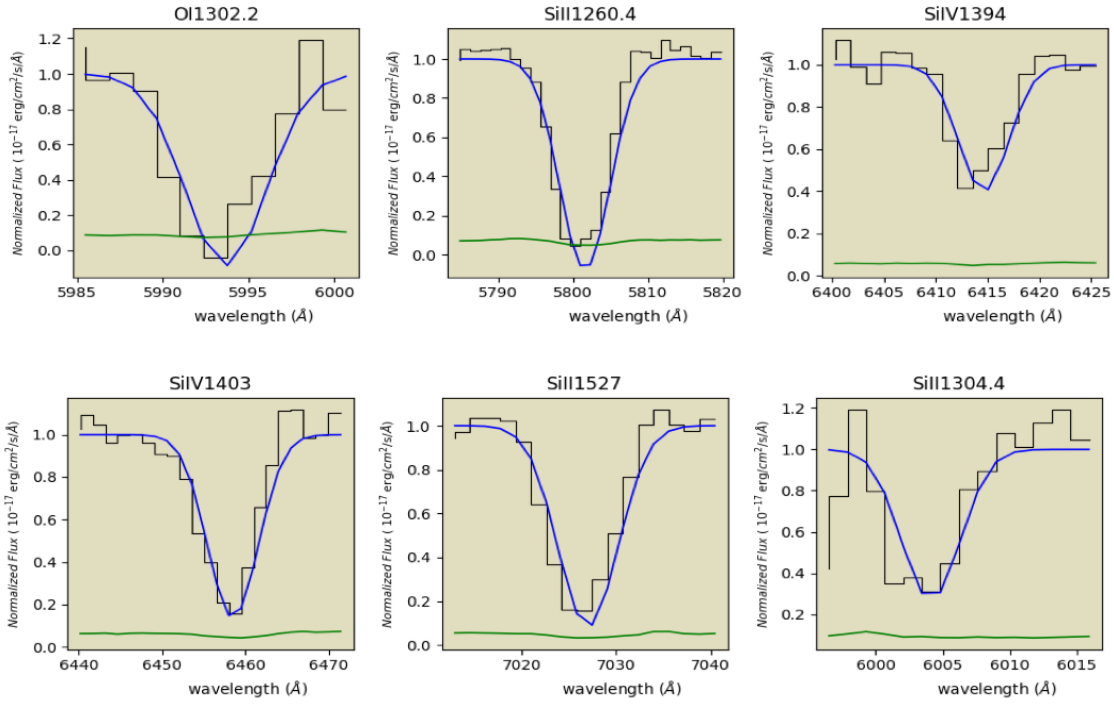

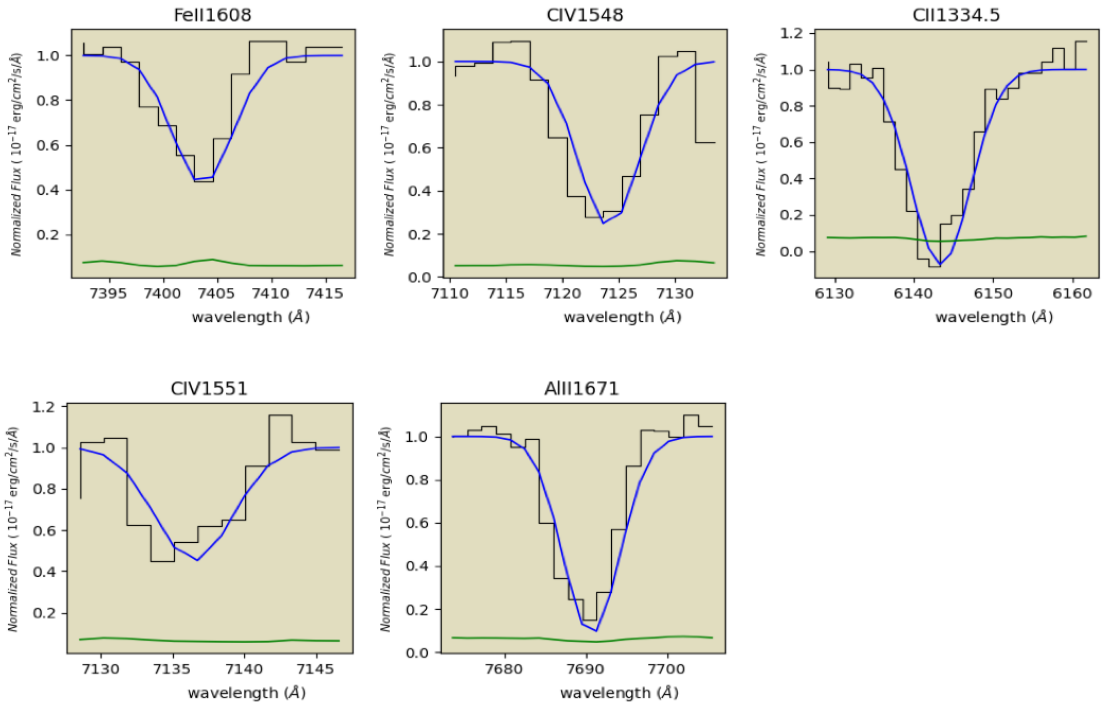

Figure 3.10 Gaussian fit for each element of z_{abs} 3.563, Wavelength (Å) vs flux (10^{-17}erg cm^{-2} s^{-1}Å^{-1})

The metallicity and relative abundances are estimated are shown in table 3.9, 3.10.

Table 3.9 Table for column density and metallicity of sightline

S.N.	Element [X]	W_X (Å)	log N_X (cm^{-2})	Metallicity [X/H]
1.	O I 1302.2	1.33	15.59	-1.35
2.	Si II 1260.4	1.82	14.39	-1.37
3.	Si II 1304.4	0.96	15.06	-0.7
4.	C II 1334.5	1.79	15.39	-1.29
5.	Si IV 1394	0.79	14.08	-1.68
6.	Si IV 1403	1.44	14.75	-1.01
7.	Si II 1527	1.54	15.02	-0.74
8.	C IV 1548	1.19	14.66	-2.02
9.	C IV 1551	0.84	14.75	-1.93
10.	Fe II 1608	0.80	14.89	-0.86
11.	Al II 1671	1.59	13.81	-0.89

Table 3.10 Relative abundance of sightline

S.N.	Relative Abundance $\left[\frac{X}{Y}\right]$
1.	$\left[\frac{\text{C II}}{\text{O I}}\right] = 0.06$
2.	$\left[\frac{\text{Fe II}}{\text{O I}}\right] = 0.49$
3.	$\left[\frac{\text{Si II}}{\text{C II}}\right] = -0.08$
4.	$\left[\frac{\text{Si II}}{\text{O I}}\right] = -0.02$

Absorber at z_{abs} =3.611 along the line of sight to J0821+4022

The absorber system z_{abs} of sightline towards the J0821+4022 is selected to study physical and chemical properties by using ions mentioned in Table 3.3. This is the lowest redshift in our selection list.

The Figures 3.11 a and b are the Voigt profile fitting program VoigtFit of the absorber system in order to determine column density of neutral Hydrogen (H I 1216). The profile is fitted with the column density 20.1 ± 0.2 dex, which is considered as sub-DLA according to Table 3.1.

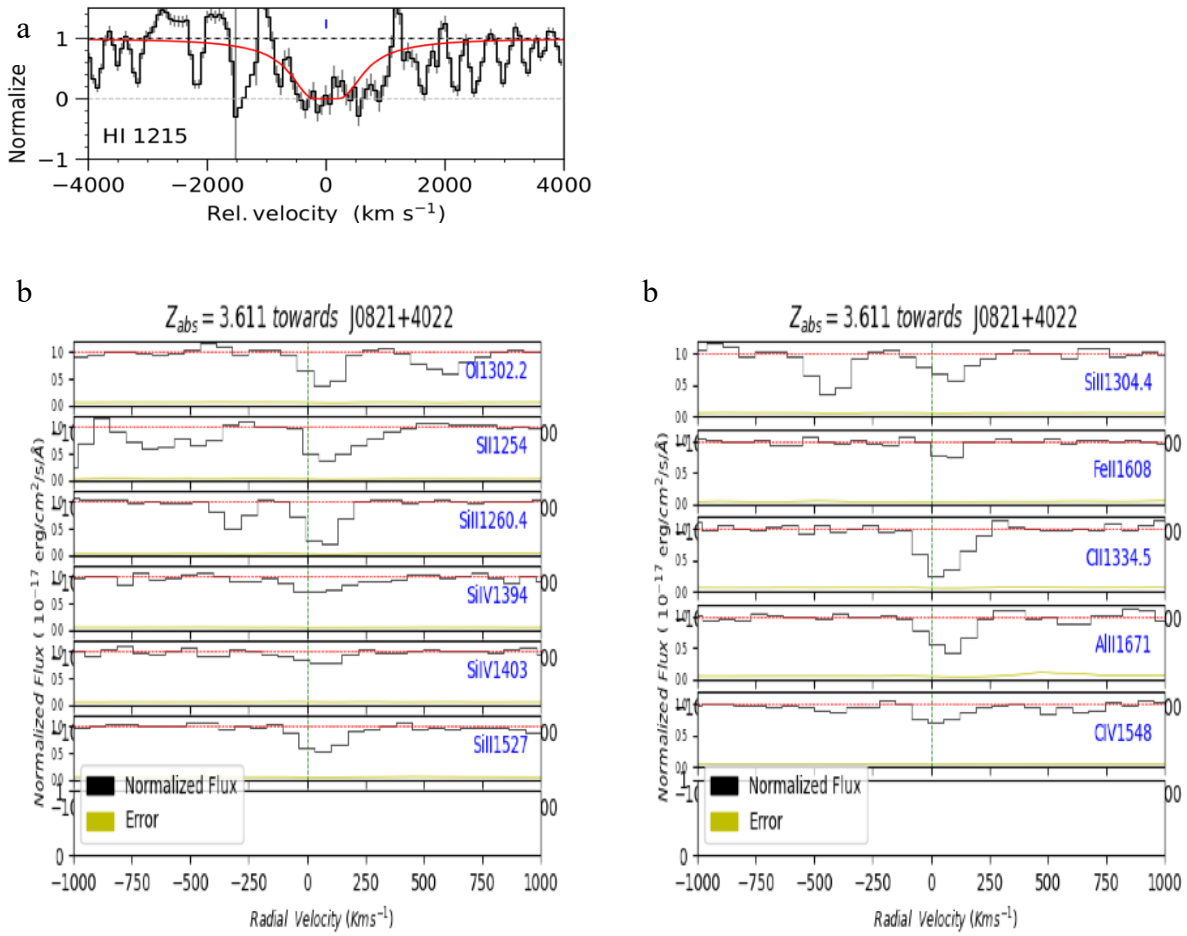

Figure 3.11 a. Voigt Profile fit of Lyman-α for DLAs with z_{abs}= 3.611 b. Radial velocity for system z_{abs}

Now from the study of the all the ions in the absorber's sightline, first we normalized flux and check if there are any unfit ions in order to sorted out from the well fitted ions with linetools. From the Figure 3.11 b is the fitted plot for ions O I 1302.2, S II 1254, Si II 1260.4, Si IV 1394, Si IV 1403, Si II 1527, Si II 1304.4, C II 1334.5, C IV 1548, Fe II 1608 and Al II 1671 are detected in the system z_{abs} = 3.611. As Si II 1260.4, Si IV 1394, Si IV 1403, Fe II 1608 and C IV 1548 is taking unusual area this ion will be neglected for further study. Remaining 6 ions are analyzed as below Figure 3.12.

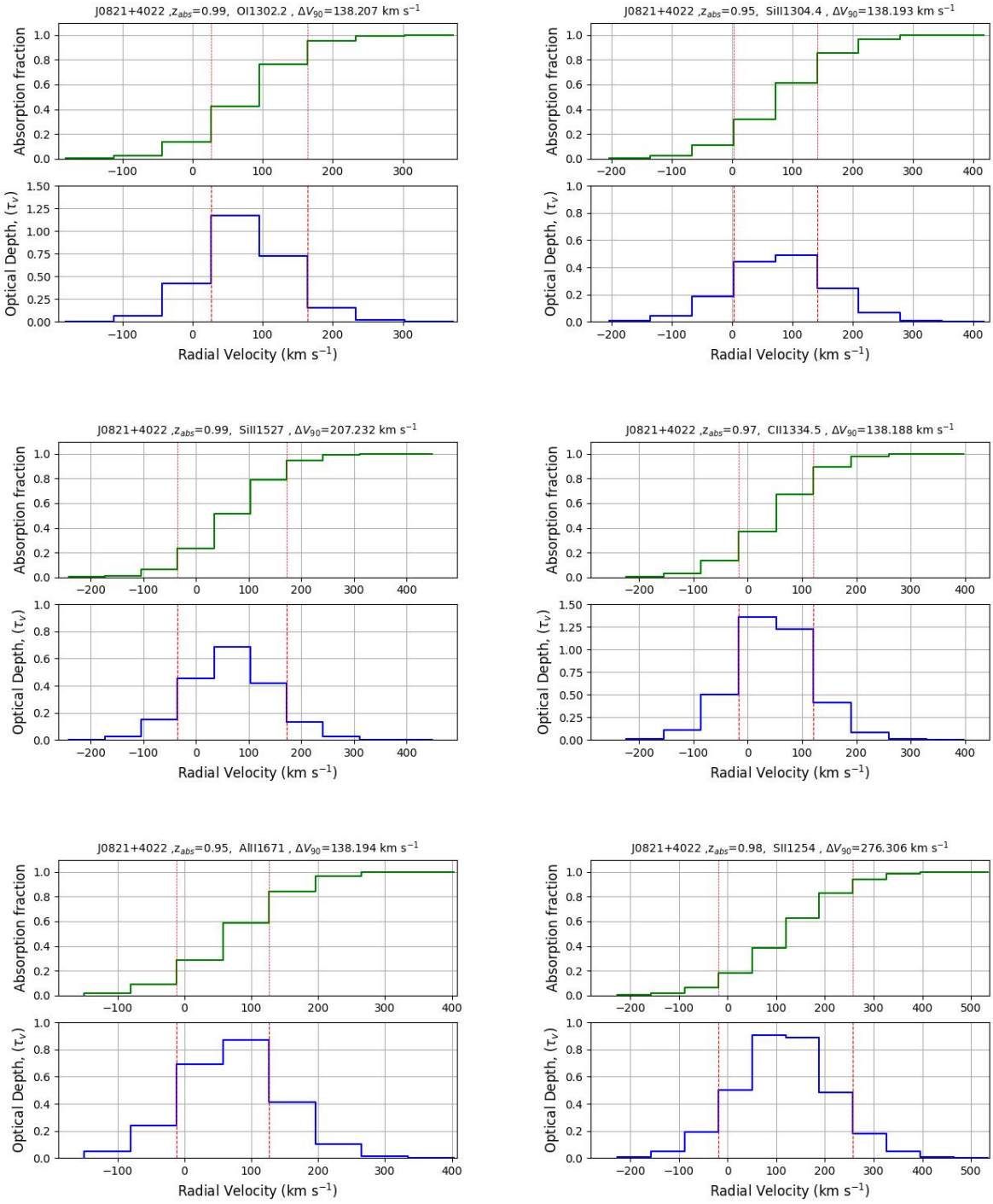

Figure 3.12 Radial velocity vs Optical Depth and absorption fraction with reference given elements

Optical depth and velocity width of selected 6 ions O I 1302.2, S II 1254, Si II 1304.4, C II 1334.5, Si II 1527 and Al II 1671 are studied and the values obtained are presented in Table 3.11 below. The observed sightline suggested it is optically thin sub-DLA system.

Table 3.11 Velocity dispersion and optical depth of absorber z_{abs} = 3.602 sightline

S.N.	Element	Velocity Width (km/s)	Optical Depth
1.	O I 1302.2	138.2	1.2
2.	S II 1254	276.3	0.9
3.	Si II 1304.4	138.2	0.5
4.	C II 1334.5	138.2	1.4
5.	Si II 1527	207.2	0.7
6.	Al II 1671	207.4	0.3

The 1-dimensional spectra absorption feature of sightline was studied and estimated the column density with help of Linetools, the calculation was done within $\pm$ 0.2 dex presented in the Figure 3.13.

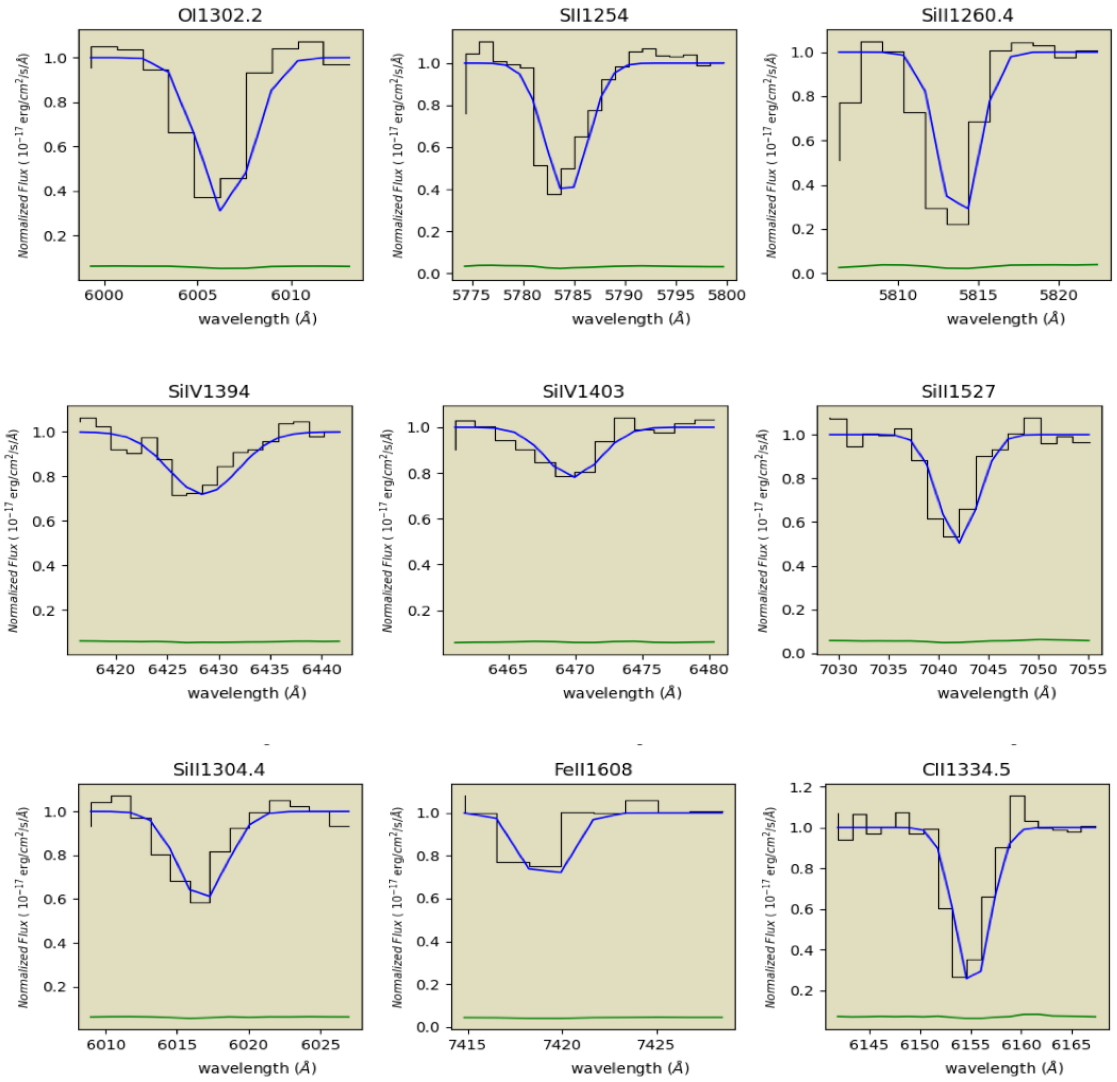

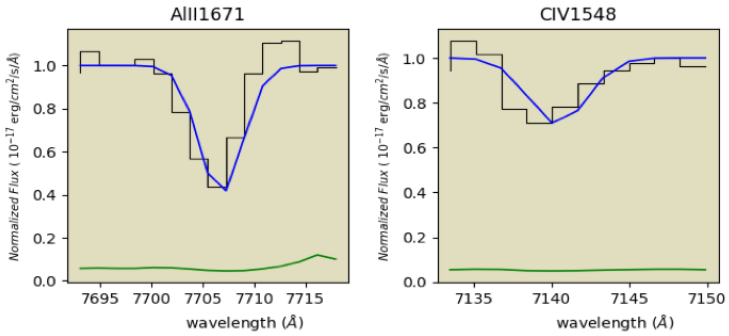

Figure 3.13 Gaussian fit for each element of z_{abs} 3.611, Wavelength (Å) vs flux (10^{-17}erg cm^{-2} s^{-1}Å^{-1})

The metallicity and relative abundances are estimated are presented in table 3.12 and 3.13.

Table 3.12 Table for column density and metallicity of sightline

S.N.	Element [X]	W_X (Å)	log N_X (cm^{-2})	Metallicity [X/H]
1.	O I 1302.2	0.48	14.99	-1.80
2.	S II 1254	0.57	14.78	-0.44
3.	Si II 1260.4	0.63	13.79	-1.82
4.	Si II 1304.4	0.41	14.53	-1.08
5.	C II 1334.5	0.73	14.76	-1.77
6.	Si IV 1394	0.52	13.78	-1.83
7.	Si IV 1403	0.25	13.84	-1.77
8.	Si II 1527	0.54	14.39	-1.22
9.	C IV 1548	0.36	13.96	-2.57
10.	Fe II 1608	0.21	14.26	-1.34
11.	Al II 1671	0.63	13.29	-1.26

Table 3.13 Relative abundance of sightline

S.N.	Relative Abundance $\left[\frac{X}{Y}\right]$
1.	$\left[\frac{\text{C II}}{\text{O I}}\right] = 0.03$
2.	$\left[\frac{\text{Fe II}}{\text{O I}}\right] = 0.46$
3.	$\left[\frac{\text{Si II}}{\text{C II}}\right] = -0.05$
4.	$\left[\frac{\text{Si II}}{\text{O I}}\right] = -0.02$
5.	$\left[\frac{\text{Si II}}{\text{S II}}\right] = -1.38$

Absorber at z_{abs} = 3.679 along the sightline to J1305+0521

The absorber system z_{abs} of sightline towards the J1305+0521 is selected to study the chemical and physical properties by using the ions mentioned in the Table 3.3. This is the lowest redshift in our selection list.

The Figure 3.14 a and b are the Voigt profile fitting program VoigtFit of the absorber system in order to determine the column density of the neutral Hydrogen (H I 1216). The profile is fitted with the column density 20.55 $\pm$ 0.2 dex, which is considered as DLA according to Table 3.1.

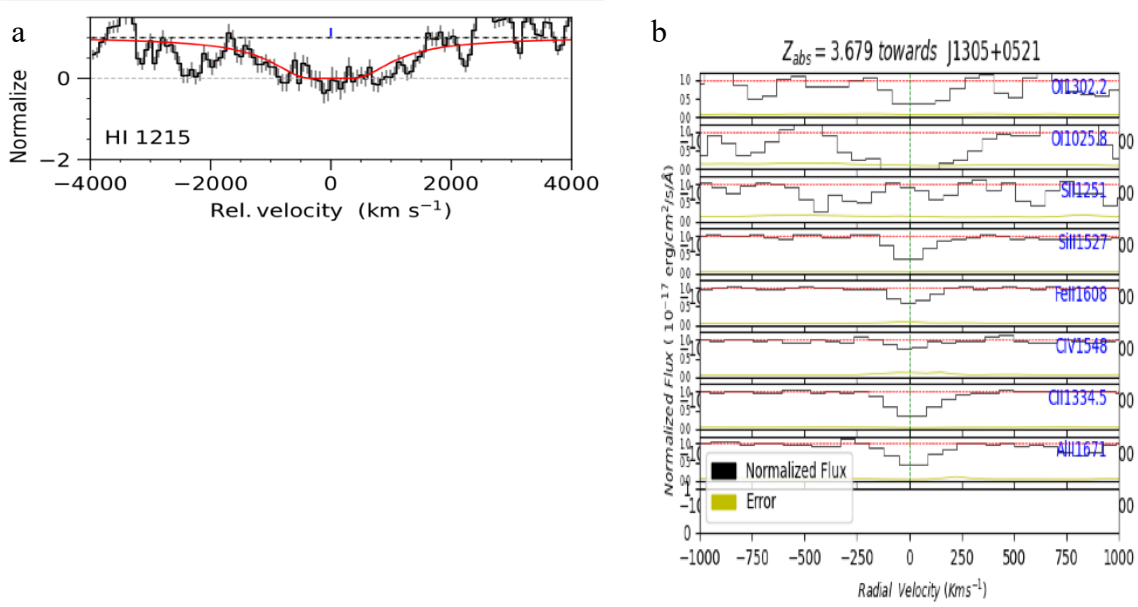

Figure 3.14 a. Voigt Profile fit of Lyman-α for DLAs with z_{abs}= 3.679 b. Radial velocity for system z_{abs}

Now from the study of the all the ions in the absorber's sightline, first we normalized flux and check if there are any unfit ions in order to sorted out from the well fitted ions with Linetools. From the Figure 3.14 b is the fitted plot for ions O I 1302.2, O I 1025.4, S II 1251, Si II 1527, C IV 1548, C II 1334.5, Fe II 1608 and Al II 1671 found in the system z_{abs} = 3.679. As O I 1025.4, S II 1551, C IV 1548, and Fe II 1608 is taking unusual area this ion will be neglected for further study. Remaining 4 ions are analyzed as below Figure 3.15

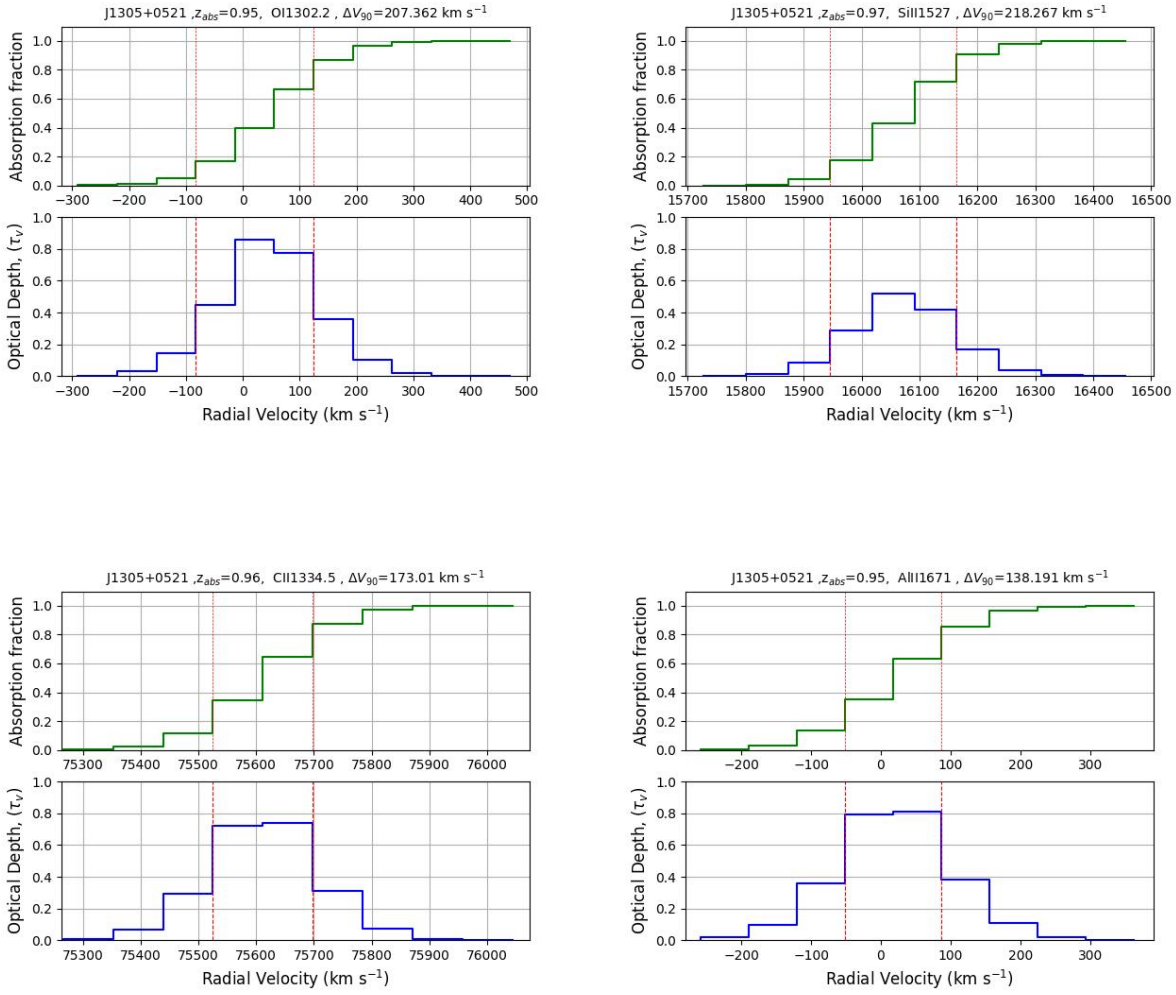

Figure 3.15 Radial velocity vs Optical Depth and absorption fraction with reference given elements

Optical depth and velocity width of selected 4 ions O I 1302.2, C II 1334.5, Si II 1527 and Al II 1671 are studied and the values obtained are presented in Table 3.14 below. The observed sightline suggested it is optically thick DLA system.

Table 3.14 Velocity dispersion and optical depth of absorber z_{abs} = 3.679 sightline

S.N.	Element	Velocity Width (km/s)	Optical Depth
1.	O I 1302.2	414.4	3.4
2.	C II 1334.5	173.1	0.7
3.	Si II 1527	218.3	0.5
4.	Al II 1671	138.2	0.8

The 1-dimensional spectra absorption feature of sightline was studied and estimated the column density with help of linetools, the calculation was done within ± 0.2 dex presented in the Figure 3.16.

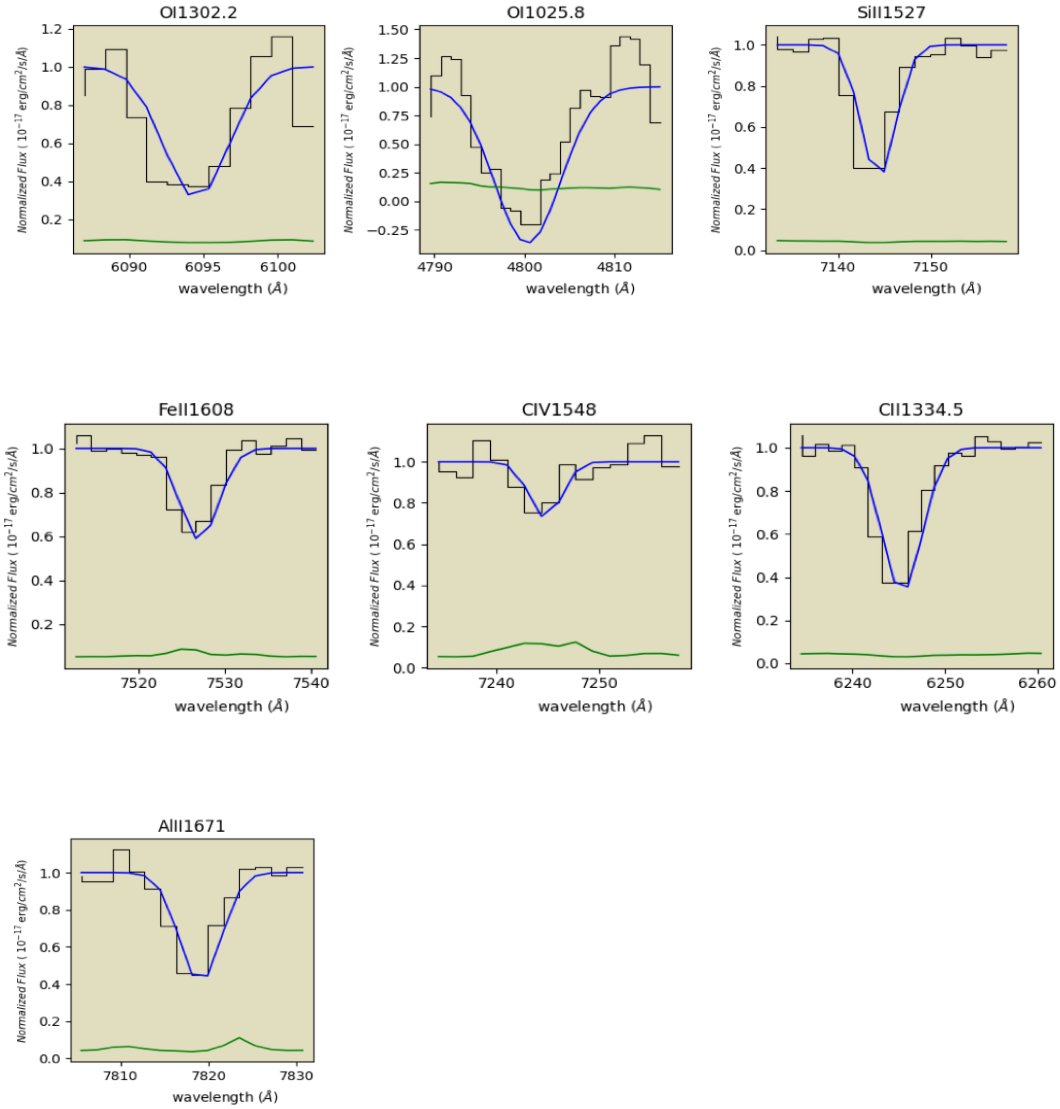

Figure 3.16 Gaussian fit for each element of z_{abs} 3.611, Wavelength (Å) vs flux (10^{-17}erg cm^{-2} s^{-1}Å^{-1})

The metallicity and relative abundances are estimated are shown in table 3.15, 3.16.

Table 3.15 Table for column density and metallicity of sightline

S.N.	Element [X]	W_X (Å)	log N_X (cm^{-2})	Metallicity [X/H]
1.	O I 1025.8	2.21	15.14	-2.09
2.	O I 1302.2	0.83	15.23	-2.01
3.	C II 1334.5	0.64	15.61	-1.37
4.	Si II 1527	0.41	14.49	-1.57
5.	C IV 1548	0.35	13.96	-3.02
6.	Fe II 1608	0.52	14.71	-1.34
7.	Al II 1671	0.81	13.41	-1.86

Table 3.16 Relative abundance of sightline

S.N.	Relative Abundance $\left[\frac{X}{Y}\right]$
1.	$\left[\frac{\text{C II}}{\text{O I}}\right] = 0.64$
2.	$\left[\frac{\text{Fe II}}{\text{O I}}\right] = 0.67$
3.	$\left[\frac{\text{Si II}}{\text{C II}}\right] = -0.19$
4.	$\left[\frac{\text{Si II}}{\text{O I}}\right] = 0.44$

Absorber at z_{abs} = 3.685 along the sightline to J1203+3411

The absorber system z_{abs} of sightline towards the J1203+3411is selected to study physical and chemical properties by using ions mentioned in Table 3.3. This is the lowest redshift in our selection list.

The Figures 3.17 a and b are the Voigt profile fitting program VoigtFit of the absorber system in order to determine column density of neutral Hydrogen (H I 1216). The profile is fitted with the column density 20.34 ± 0.2 dex, which is considered as DLA according to Table 3.1.

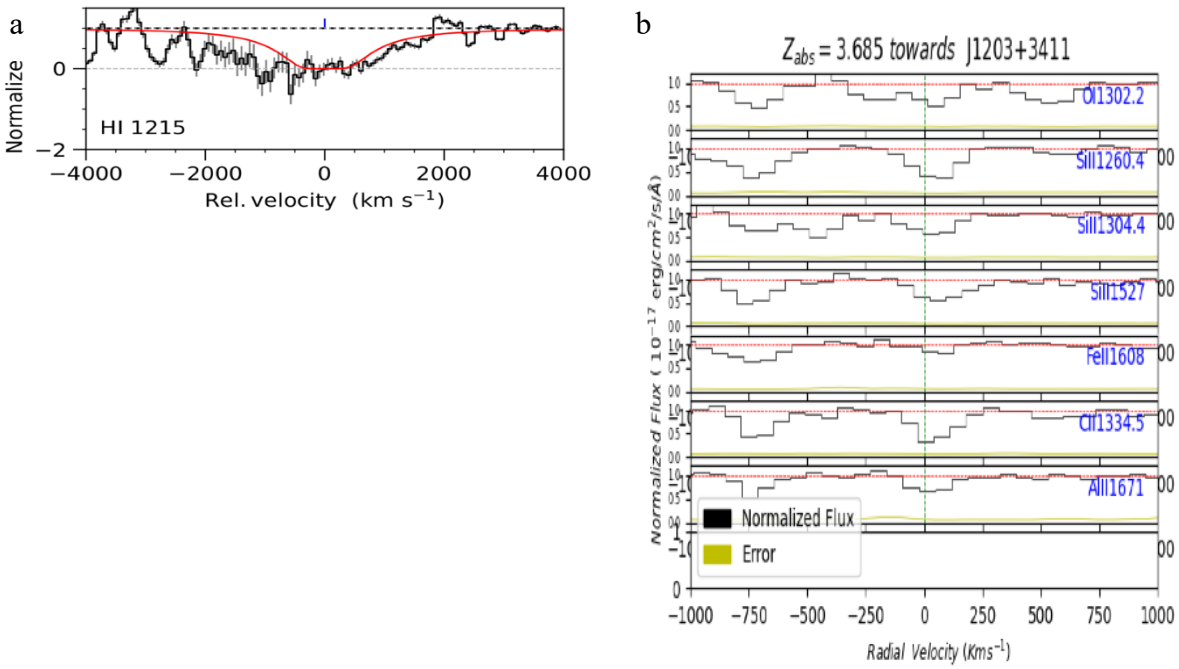

Figure 3.17 a. Voigt Profile fit of Lyman-α for DLAs with z_{abs}= 3.679 b. Radial velocity for system z_{abs}

Now from the study of the all the ions in the absorber's sightline, first we normalized flux and check if there are any unfit ions in order to sorted out from the well fitted ions with Linetools. From the Figure 3.17 b is the fitted plot for ions O I 1302.2, Si II 1260.4, Si II 1527, Si II 1304.4, C II 1334.5, Fe II 1608 and Al II 1671 found in the system z_{abs} = 3.685. As Fe II 1608 is taking unusual area this ion will be neglected for further study. Remaining 6 ions are analyzed as below Figure 3.18

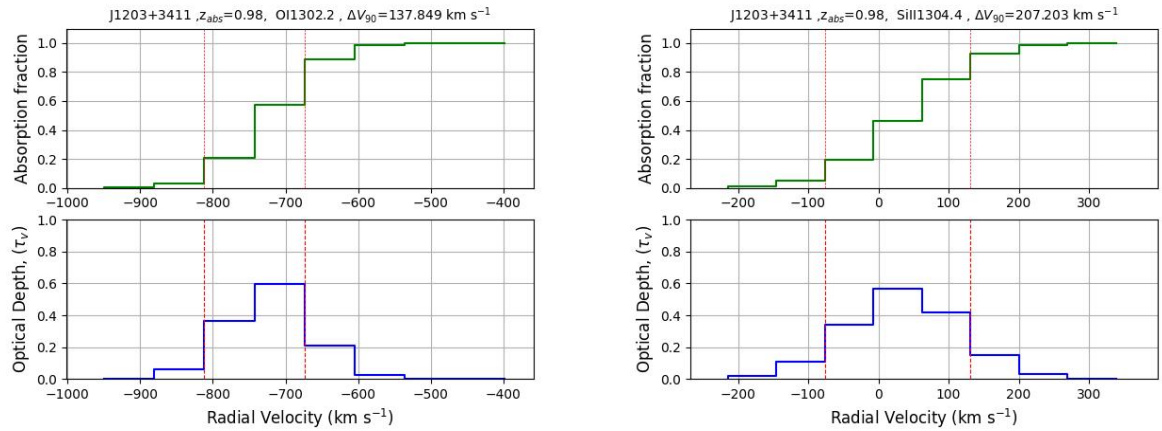

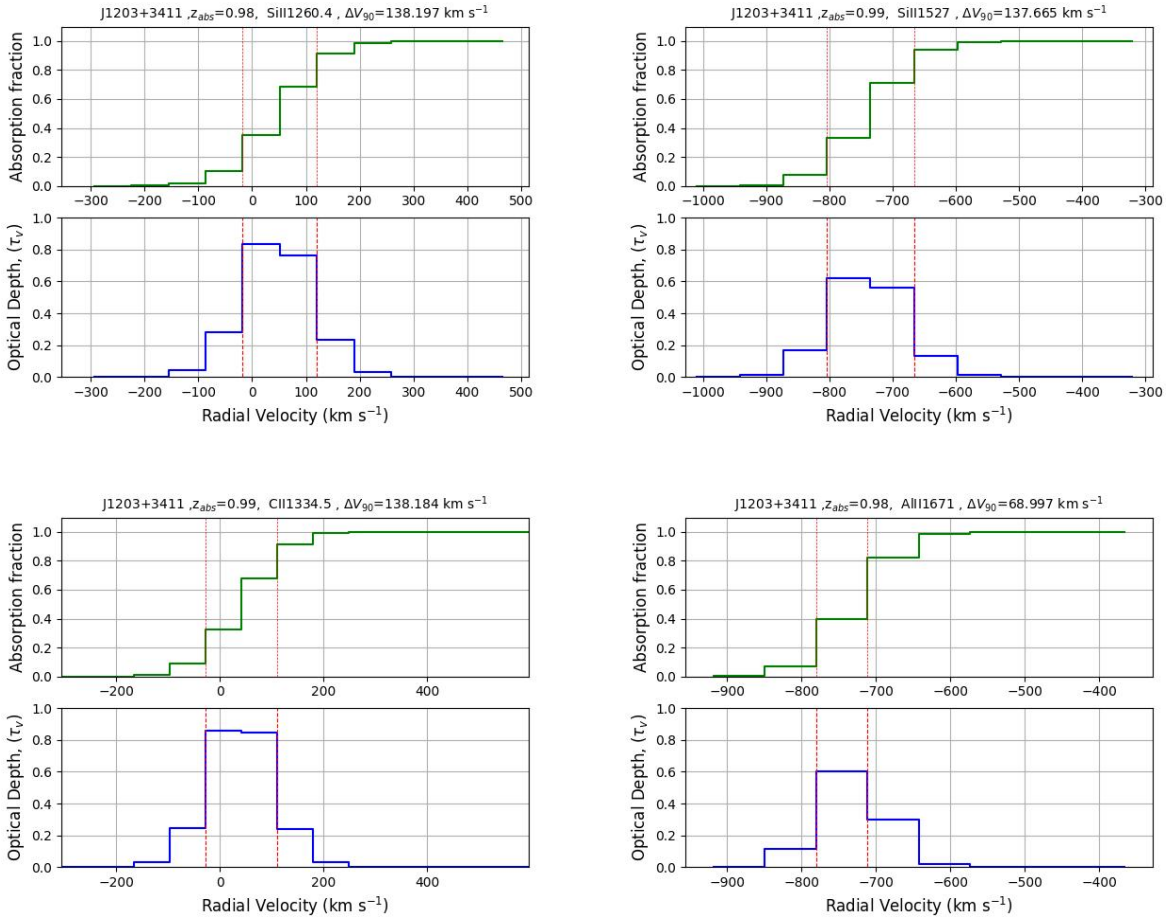

Figure 3.18 Radial velocity vs Optical Depth and absorption fraction with reference given elements

Optical depth and velocity width of selected 6 ions O I 1302.2, Si II 1260.4, Si II 1527, Si II 1304.4, C II 1334.5 and Al II 1671are studied and the values obtained are presented in Table 3.17 below. The observed sightline suggested it is optically thin DLA system.

Table 3.17 Velocity dispersion and optical depth of absorber z_{abs} = 3.685 sightline

S.N.	Element	Velocity Width (km/s)	Optical Depth
1.	O I 1302.2	137.8	0.6
2.	Si II 1260.4	138.2	0.8
3.	Si II 1304.4	207.2	0.6
4.	C II 1334.5	138.2	0.8
5.	Si II 1527	137.7	0.6
6.	Al II 1671	68.9	0.6

The 1-dimensional spectra absorption feature of sightline was studied and estimated the column density with help of Linetools, the calculation was done within $\pm$ 0.2 dex presented in the Figure 3.19.

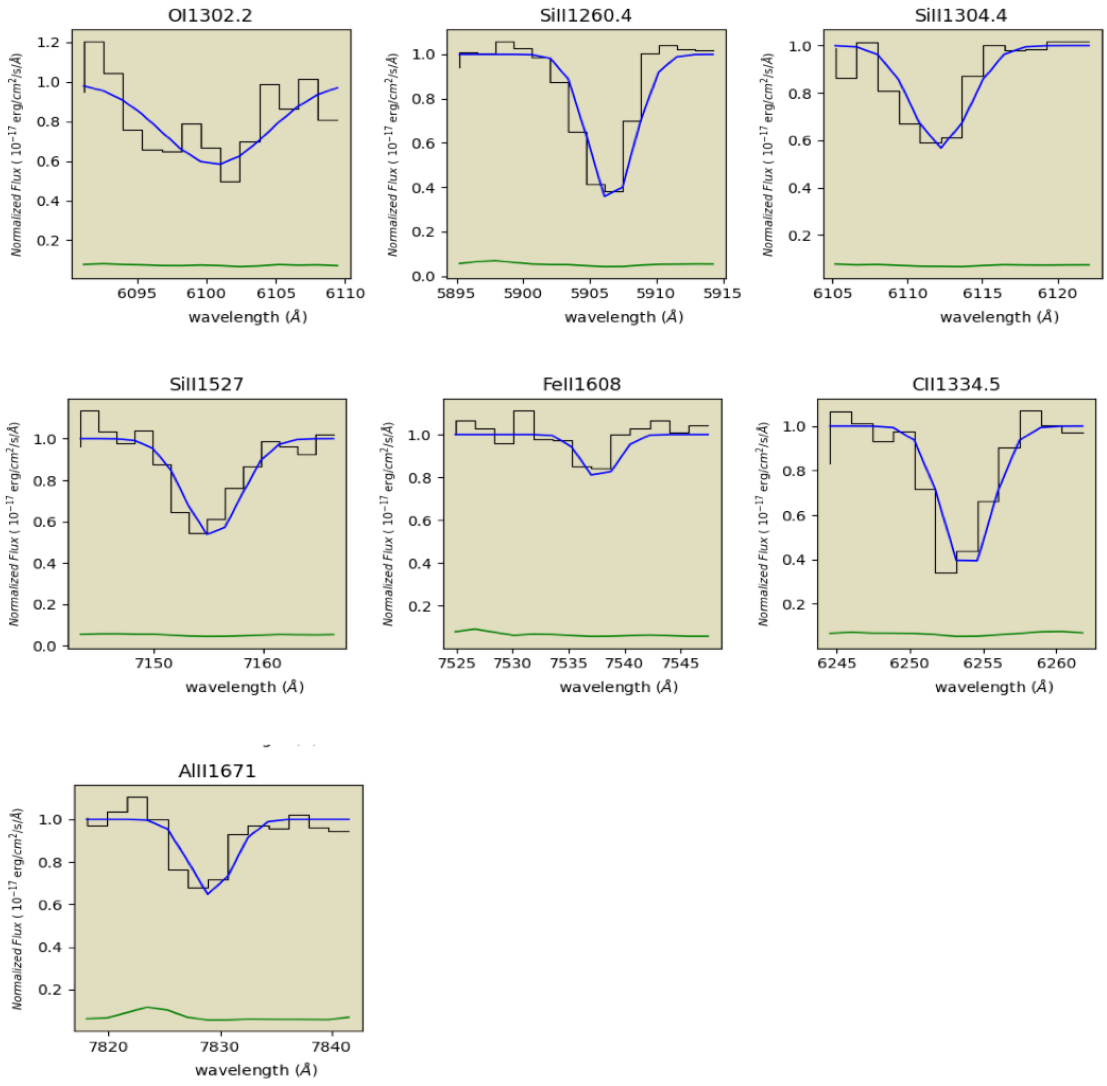

Figure 3.19 Gaussian fit for each element of z_{abs} 3.685, Wavelength (Å) vs flux (10^{-17}erg cm^{-2} s^{-1}Å^{-1})

The metallicity and relative abundances are estimated are presented in table 3.18 and 3.19.

Table 3.18 Table for column density and metallicity of sightline

S.N.	Element [X]	W_X (Å)	log N_X (cm^{-2})	Metallicity [X/H]
1.	O I 1302.2	0.74	14.01	-3.02
2.	Si II 1260.4	0.61	13.71	-2.14
3.	Si II 1304.4	0.44	14.61	-1.24
4.	C II 1334.5	0.49	14.29	-2.48
5.	Si II 1527	0.73	14.52	-1.33
6.	Fe II 1608	0.29	14.39	-1.45
7.	Al II 1671	0.39	13.01	-1.78

Table 3.19 Relative abundance of sightline

S.N.	Relative Abundance $\left[\frac{X}{Y}\right]$
1.	$\left[\frac{\text{C II}}{\text{O I}}\right] = 0.54$
2.	$\left[\frac{\text{Fe II}}{\text{O I}}\right] = 1.57$
3.	$\left[\frac{\text{Si II}}{\text{C II}}\right] = 0.34$
4.	$\left[\frac{\text{Si II}}{\text{O I}}\right] = 0.88$

Absorber at z_{abs} = 4.31 along the sightline to J1050+4411

The absorber system z_{abs} of sightline towards the J1050+4411 is selected to study the chemical and physical properties by using the ions mentioned in the Table 3.3. This is the lowest redshift in our selection list.

The Figures 3.20 a and b are the Voigt profile fitting program VoigtFit of the absorber system in order to determine the column density of the neutral Hydrogen (H I 1216). The profile is fitted with the column density 20.35 $\pm$ 0.2 dex, which is considered as DLA according to Table 3.1.

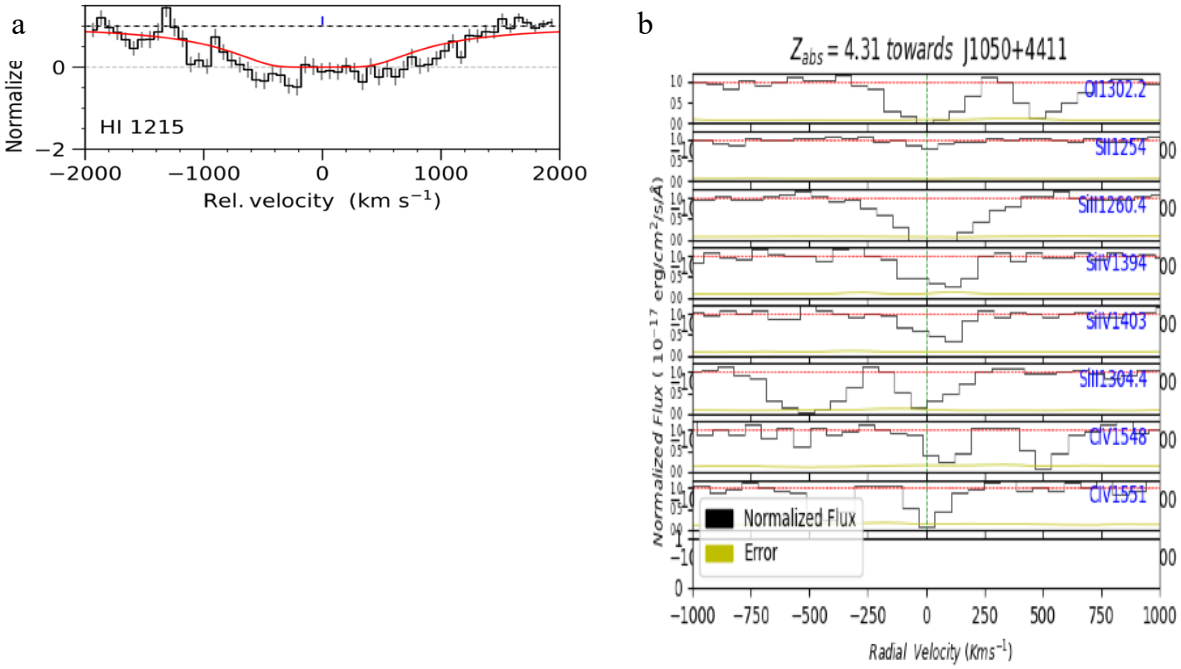

Figure 3.20 a. Voigt Profile fit of Lyman-α for DLAs with z_{abs}= 4.31 b. Radial velocity for system z_{abs}

Now from the study of the all the ions in the absorber's sightline, first we normalized flux and check if there are any unfit ions in order to sorted out from the well fitted ions with Linetools. From the Figure 3.20 b is the fitted plot for ions O I 1302.2, S II 1254, Si II 1260.4, Si IV 1394, Si IV 1403, Si II 1304.4, C IV 1548 and C IV 1551 found in the system z_{abs} = 4.31. As S II 1254 is taking unusual area this ion will be neglected for further study. Remaining 6 ions are analyzed as below Figure 3.21.

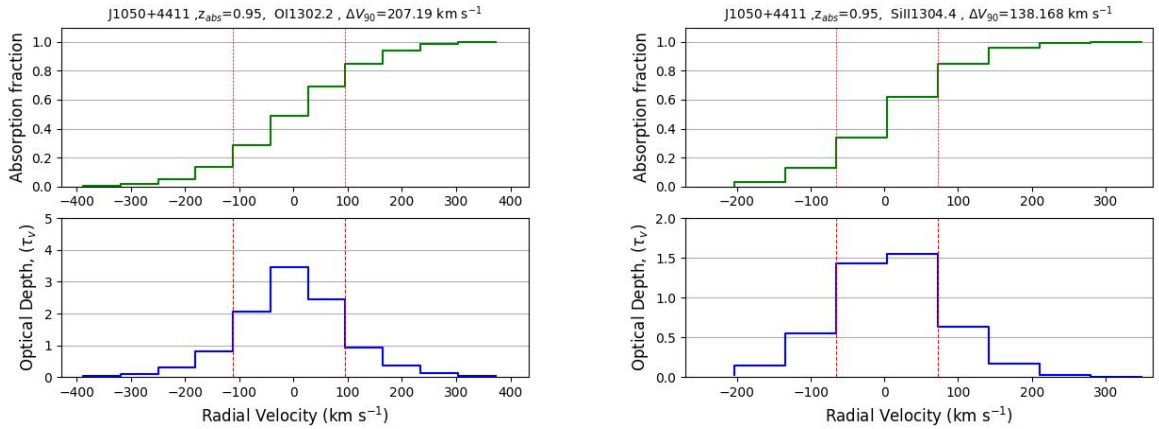

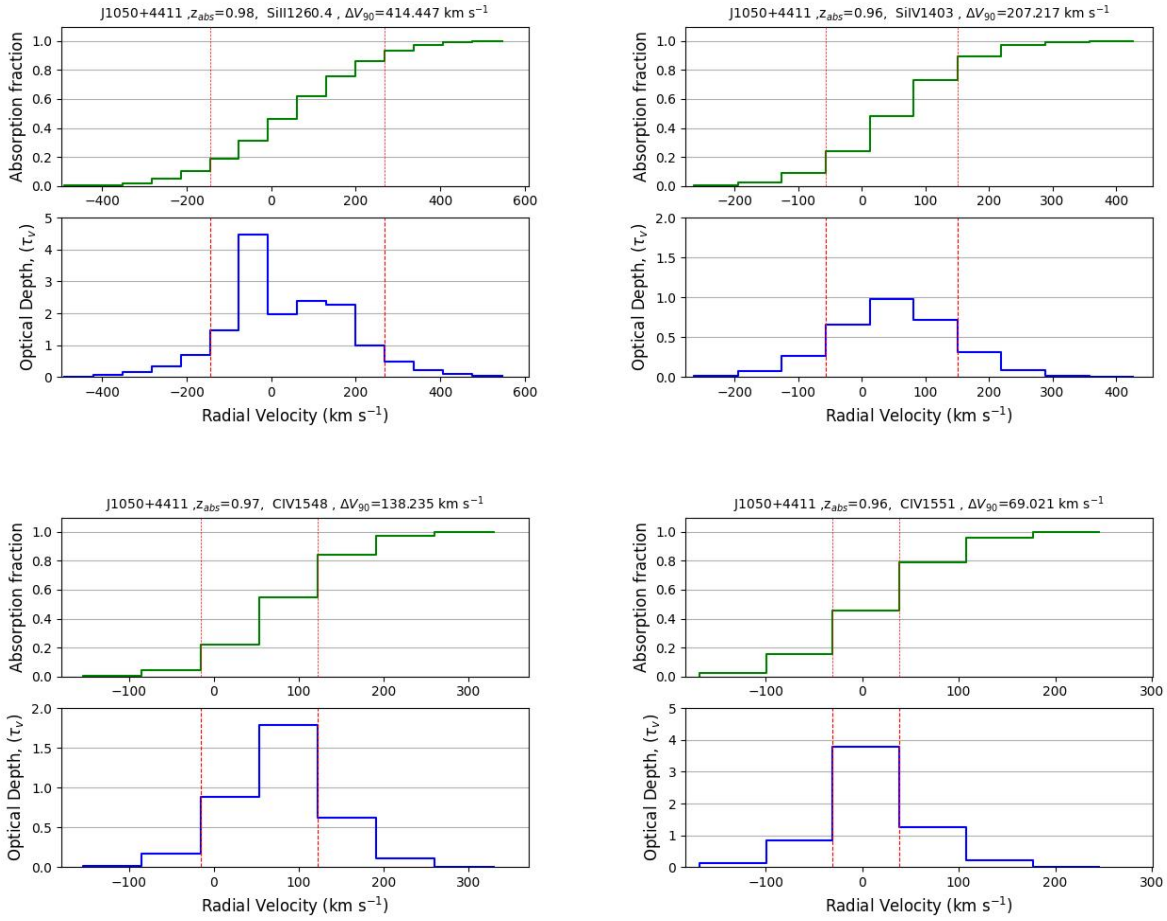

Figure 3.21 Radial velocity vs Optical Depth and absorption fraction with reference given elements

Optical depth and velocity width of selected 6 ions O I 1302.2, Si II 1260.4, Si IV 1394, Si IV 1403, Si II 1304.4, C IV 1548 and C IV 1551 are studied and the values obtained are presented in table 3.5 below. The observed sightline suggested it is optically thick DLA system.

Table 3.20 Velocity dispersion and optical depth of absorber z_{abs} = 4.31 sightline

S.N.	Element	Velocity Width (km/s)	Optical Depth
1.	O I 1302.2	207.2	3.5
2.	Si II 1260.4	414.4	4.5
3.	Si II 1304.4	138.2	1.6
4.	Si IV 1403	207.2	0.9
5.	C IV 1548	138.2	1.8
6.	C IV 1551	68.1	3.8

The 1-dimensional spectra absorption feature of sightline was studied and estimated the column density with help of Linetools, the calculation was done within $\pm$ 0.2 dex presented in the Figure 3.22.

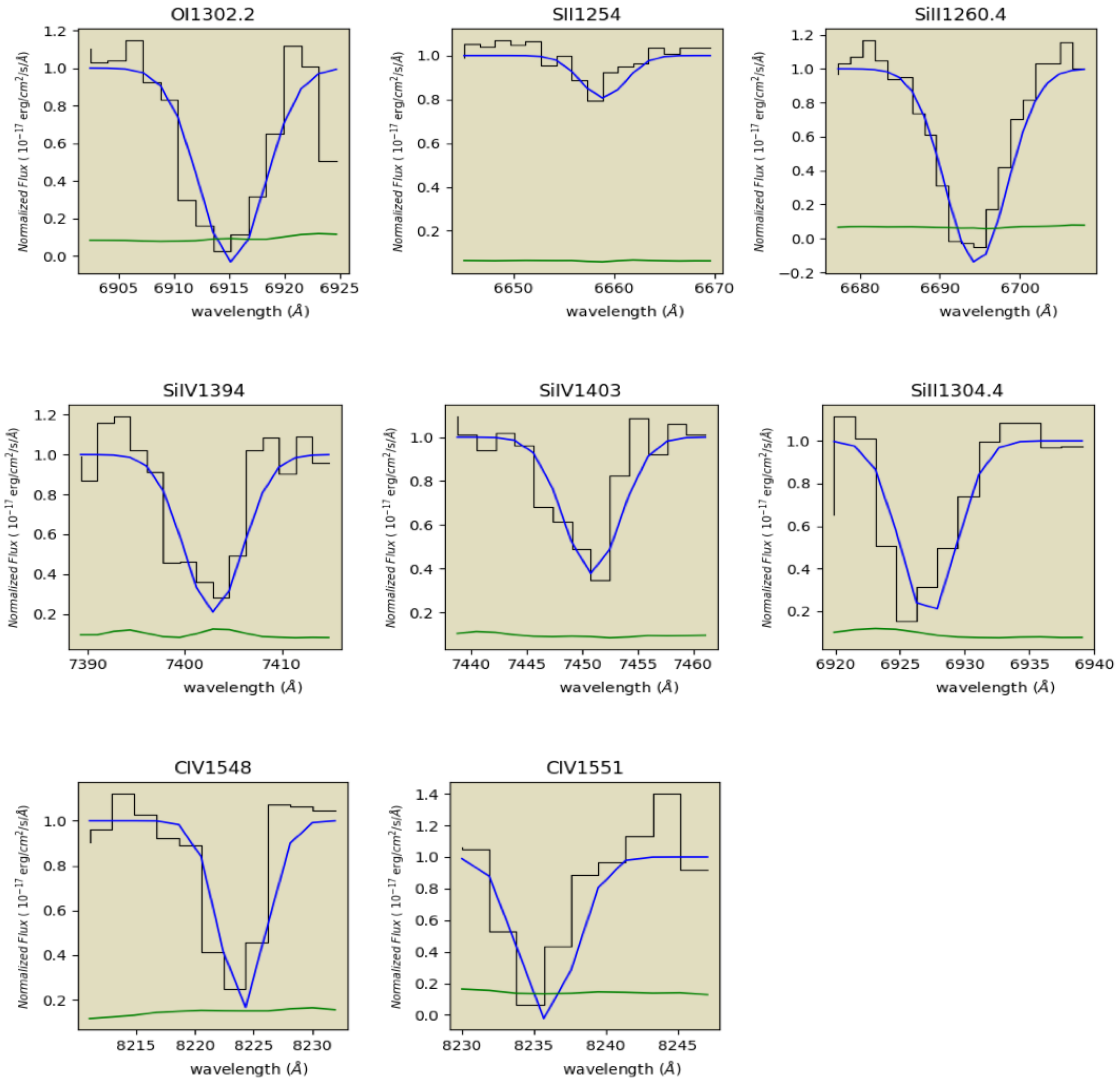

Figure 3.22 Gaussian fit for each element of z_{abs} 3.685, Wavelength (Å) vs flux (10^{-17}erg cm^{-2} s^{-1}Å^{-1})

The metallicity and relative abundances are estimated are shown in table 3.21, 3.22.

Table 3.21 Table for column density and metallicity of sightline

S.N.	Element [X]	W_X (Å)	log N_X (cm^{-2})	Metallicity [X/H]
1.	O I 1302.2	1.45	15.63	-1.41
2.	S II 1254	0.18	15.41	-0.06
3.	Si II 1260.4	1.89	14.41	-1.45
4.	Si II 1304.4	0.84	15.04	-0.82
5.	Si IV 1394	1.04	14.26	-1.60
6.	Si IV 1403	0.69	14.31	-1.55
7.	C IV 1548	0.74	14.51	-2.27
8.	C IV 1551	0.77	14.91	-1.87
9.	Fe II 1608	0.34	14.54	-1.31

Table 3.22 Relative abundance of sightline

S.N.	Relative Abundance $\left[\frac{X}{Y}\right]$
1.	$\left[\frac{\text{Si II}}{\text{O I}}\right] = -0.04$
2.	$\left[\frac{\text{Si II}}{\text{S II}}\right] = -1.39$
3.	$\left[\frac{\text{Fe II}}{\text{O I}}\right] = 0.09$

In summary, we followed the following chronological steps to determine abundances:

1. Selection of the data from SDSS and Data reduction.
2. 1-dimensional spectra extracted.
3. Determined the absorbers' redshift based on the metal lines of Table 3.3 using determined H I column density using Voigt profile fitting program VoigtFit and estimate the equivalent widths and metal column densities fitting Gaussian and applying apparent optical depth (AOD) method with the help of spectra analysis tool called Linetools.
4. Calculation of the velocity width, optical depth, equivalent width, column density, metallicity and relative abundances.

CHAPTER 4

RESULT AND DISCUSSION

From the available quasar spectra, after carefully analyzed each spectrum with Voigt profile fitting program VoigtFit and Linetools, we were able to present 6 relatively proper system with corrected H I 1216 column densities are presented in Table 4.1. The values of log $N_{H\,I}$ are different from the reported by Noterdaeme et al. (2012) and we found J0811+3727, J1015+3921 and J0821+4022 are sub-DLAs and J1305+0521, J1203+3411 and J1050+4411 are DLAs shown in Table 4.1.

Table 4.1 Comparative representation of observed column density of selected sightlines

S.N.	QSO name	RA (J2000)	DEC (J2000)	log $N_{H\,I}$ Reported (Noterdaeme et al. (2012)) (cm^{-2})	log $N_{H\,I}$ Calculated (cm^{-2})
1.	J0811+3727	081132.2100	+372755.440	20.66	20.1 ± 0.2
2.	J1015+3921	101526.3300	+392107.200	20.69	20.25 ± 0.2
3.	J0821+4022	082159.5900	+402236.480	20.53	20.1 ± 0.2
4.	J1305+0521	130502.2800	+052151.120	21.17	20.55 ± 0.2
5.	J1203+3411	120359.0700	+341114.290	20.92	20.34 ± 0.2
6.	J1050+4411	105049.2800	+441144.880	20.35	20.35 ± 0.2

Table 4.2 summarized the relative abundances of all 6 sightlines with [C IV/O I], [Fe II/ O I], [Si II/C IV], [Si II/O I], [C II/O I], [Si II/C II] and [Si II/S II].

Table 4.2 Summary table of relative abundances and ratio of column density of C IV to Si IV of all selected absorber systems

S.N.	QSO and Absorption Systems	$\left[\frac{\text{Fe II}}{\text{O I}}\right]$	$\left[\frac{\text{Si II}}{\text{O I}}\right]$	$\left[\frac{\text{C II}}{\text{O I}}\right]$	$\left[\frac{\text{Si II}}{\text{C II}}\right]$	$\left[\frac{\text{Si II}}{\text{S II}}\right]$	$\frac{\text{N (C IV)}}{\text{N (Si IV)}}$
1.	J0811+3727 z_{abs} = 3.563 $\log N_{H\,I}$ 20.1± 0.2	0.54	0.04				1.82
2.	J1015+3921 z_{abs} = 3.602 $\log N_{H\,I}$ 20.25 ± 0.2	0.49	−0.02	0.06	−0.08		1.95
3.	J0821+4022 z_{abs} = 3.611 $\log N_{H\,I}$ 20.1 ± 0.2	0.46	−0.02	0.03	−0.05	−1.38	1.41
4.	J1305+0521 z_{abs} = 3.679 $\log N_{H\,I}$ 20.55 ± 0.2	0.67	0.44	0.64	−0.19		
5.	J1203+3411 z_{abs} = 3.685 $\log N_{H\,I}$ 20.34 ± 0.2	1.57	0.88	0.54	0.34		6.46
6.	J1050+4411 z_{abs} = 4.31 $\log N_{H\,I}$ 20.35 ± 0.2	0.09	−0.04			−1.39	2.63

Absorber at z = 3.563 along the sightline to J0811+3727

The negative value of [C IV/O I] i.e., -0.58 seems like C IV is underabundant relative to O I. This also satisfy the limit of nucleosynthesis model (Cooke, Pettini, & Steidel, 2017). But the limit for [Si II/O I] cannot be satisfactory due to its small value i.e., 0.04. The metallicity [Fe II/H I] is -0.75 indicates this system may be affected by the pair instability supernovae from population I stars (Heger & Woosley, 2002, Cooke, Pettini, & Steidel, 2017) in the early universe after Big Bang.

Absorber at z = 3.602 along the sightline to J1015+3921

For this sightline, Si II is almost equal to O I. The value of [C IV/O I] abundances is -0.67, which so less that shows Carbon is not abundant in the system. Here metallicity [Fe II/H I] is -0.86. As there is lower metallicity from Population I stars (Heger & Woosley, 2002, Cooke, Pettini, & Steidel, 2017).

Absorber at z =3.611 along the sightline to J0821+4022

The unique feature of this system is we have detected Sulphur and [Si II/S II] ratio is -1.38. The [Si II/C IV] and [Si II/O I] ratio gives the abundant of Silicon relative to Oxygen and Carbon respectively and negative value of [Si II/S I] may be due to the high condensation temperature of Sulphur than that of Carbon and Oxygen. Here metallicity [Fe II/H I] is -1.34. This belongs to the Population II stars (Heger & Woosley, 2002, Cooke, Pettini, & Steidel, 2017).

Absorber at z = 3.679 along the sightline to J1305+0521

The [Si/O] ratio satisfy the condition for the early Stars and [C/O] doesn't satisfy this condition. This may be due to the both Oxygen and Carbon are near the Saturated point as shown in Gaussian fit. Here metallicity [Fe II/H I] is -1.342 which is out of the limit mentioned in table 1.2 so this system may be affected from Population II stars (Heger & Woosley, 2002, Cooke, Pettini, & Steidel, 2017) which may have undergone pair-instability supernovae.

Absorber at z = 3.685 along the sightline to J1203+3411

Among all the system we found greater abundances [Si/O], [Fe/O], [C/O] altogether. This means this include depletion of metal Fe, C, Si including less abundances of oxygen. Here metallicity [Fe II/H I] is -1.45. As this is lower metallicity, we can guess this system may be affected from Population II stars (Heger & Woosley, 2002, Cooke, Pettini, & Steidel, 2017).

Absorber at z = 4.31 along the sightline to J1050+4411

The unique feature of this system is we have detected Sulphur and [Si II/S II] ratio is -1.39. The [Si II/C IV] and [Si II/O I] ratio gives the abundant of Silicon relative to Oxygen and Carbon respectively and negative value of [Si II/S I] may be due to the high condensation temperature of Sulphur than that of Carbon and Oxygen. Here [Fe II/H I] is -1.26, this system is also likely from population II stars (Heger & Woosley, 2002, Cooke, Pettini, & Steidel, 2017).

CHAPTER 5

CONCLUSIONS AND FUTURE WORK

5.1 CONCLUSIONS

We have studied 6 new sightlines of metal absorbers at redshift range $3 \lesssim z_{abs} \lesssim 5$ using SDSS data. Our observations have found three new sub-DLAs and three new DLAs metallicity providing improved constraints on evolution of gas-rich galaxies at these redshift regimes. Combining our data with those for sub-DLAs and DLAs from the literature, we studied various chemical and kinematic properties. The main conclusions derived from this work are summarized as follows:

1. Equivalent width of each system with detection level more than are 3 σ are given priorities to confirm the column density estimation within cosmological redshift of $3 \lesssim z_{abs} \lesssim 5$.
2. We found 3 new DLAs with neutral hydrogen column densities log $N_{H\,I}$ (cm^{-2}) = 20.55 $\pm$ 0.2, 20.34 $\pm$ 0.2, 20.35 $\pm$ 0.2 and 3 new sub-DLAs with neutral hydrogen column densities log $N_{H\,I}$ (cm^{-2}) = 20.1$\pm$ 0.2, 20.25 $\pm$ 0.2, 20.1 $\pm$ 0.2 with multiple ions detected.
3. We have measured at least three parameters for all the sightlines i.e., 1. [Fe/H] 2. velocity dispersion 3. For 4 out of 6 sightlines, the measured [Si/O] values are consistent with solar and for the rest of the two sightlines these values are super solar at ~0.4 and ~0.9, respectively. For those sightlines with super solar [Si/O], we also observed super solar [C/O]. These values are different than the typical metal-poor DLAs. They may be the signatures of unusual nucleosynthesis from early stars (Huyan et al., 2023).
4. J0811+3727 and J1015+3921 are population I stars (metal rich) whereas J1305+0521 and J1203+3411, J0821+4022 and J1050+4411 are population II stars (metal poor) (Cooke, Pettini, & Steidel, 2017).
5. J0811+3727 has the highest velocity dispersion with respect to metallicity. If the velocity dispersion is taken as a proxy of mass of a galaxy (Péroux et. al. 2003, Ledoux et al. 2006), this may suggest the dominance of dark matter halo in this system (Poudel et al. 2018, 2019). We detected higher abundance for Sulphur in J0821+4022 and J1050+4411 which also supports to infer the depletion of Silicon in the corresponding systems (De Cia et al., 2016, 2018, Poudel et al. 2018, 2019).

6. We also detect C IV and Si IV absorption signifying that the collisional ionization may be prevalent in these DLAs/sub-DLAs. The column density ratios of N (C IV)/N (Si IV) are in the range of 1.4 – 6.5, signifying these absorbers may be ionized by both the photoionization and collisional ionization.

Thus, observations of DLAs and sub-DLAs in quasar absorber line systems reveal intriguing differences. Beyond variations in their neutral hydrogen (H I) column densities, DLAs and sub-DLAs exhibit distinct characteristics related to gas kinematics, stellar populations, and metallicity. It is likely that DLAs, which are metal-poor and gas-rich, detecting various galaxy populations than sub-DLAs, which are metal-rich but gas-poor. By studying these properties across cosmic time, researchers can gain valuable understanding of the underlying processes propelling galaxy evolution.

5.2 FUTURE WORK

Noterdaeme et al. (2012) had utilized data released from SDSS Survey-III Data Release 9 to identify 12081 systems with log $N_{H\,I}$ (cm^{-2}) ≥ 20, out of which 6839 have log $N_{H\,I}$ (cm^{-2}) ≥ 20.3. We will use latest publicly available of quasar spectra from SDSS for identifying DLAs. We will select the systems with equivalent width, W (Mg II 2796) > 0.3 Å as a proxy for DLAs as the systems with strong Mg II 2796 absorptions are often probe the DLAs (Rao et al. 2017). Furthermore, we will explore machine learning technique as there are hundreds of confirmed DLAs systems in the literature which can be used as a test sample. We will estimate equivalent width and column density of absorbers and compare with results from Noterdaeme et al. (2012) and also with high-resolution data from literatures such as Poudel et al. (2018, 2020), Prochaska et al. (2003a, 2003b) and Som et al. (2015), also we will make it possible to calculate all spectra and characterization of metallicities and relative abundances, in order to study C IV 1548 vs C II 1334 photoionization plus collisional ionization in CGM. the columns contain Fe II 1608, Si II 1526 and C II 1334 along with their corresponding errors to study O I 1302 vs Fe II 1608 dust depletion in CGM.

REFERENCES

Asplund, M., Grevesse, N., Sauval, A. J., & Scott, P. (2009). The Chemical Composition of the Sun. *Annual Review of Astronomy and Astrophysics*, *47*(1), 481–522. https://doi.org/10.1146/annurev.astro.46.060407.145222

Becker, G. D., Bolton, J. S., & Lidz, A. (2015). Reionisation and High-Redshift Galaxies: The View from Quasar Absorption Lines. *Publications of the Astronomical Society of Australia*, *32*(e045). https://doi.org/10.1017/pasa.2015.45

Cimatti, A., Filippo Fraternali, & Nipoti, C. (2020). *Introduction to galaxy formation and evolution: from primordial gas to present-day galaxies*. Cambridge, United Kingdom; New York, Ny, Usa: Cambridge University Press.

Cooke, R., Pettini, M., & Steidel, C. C. (2017). Discovery of the most metal-poor damped Lyman-α system. *Monthly Notices of the Royal Astronomical Society*, *467*(1), stx037–stx037. https://doi.org/10.1093/mnras/stx037

De Cia, A., Ledoux, C., Mattsson, L., Petitjean, P., Srianand, R., Gavignaud, I., & Jenkins, E. B. (2016). Dust-depletion sequences in damped Lyman-*α*absorbers. *Astronomy & Astrophysics (A&A)*, *596*(A97), A97–A97. https://doi.org/10.1051/0004-6361/201527895

De Cia, A., Ledoux, C., Petitjean, P., & Savaglio, S. (2018). The cosmic evolution of dust-corrected metallicity in the neutral gas. *Astronomy & Astrophysics (A&A)*, *611*(A76), A76–A76. https://doi.org/10.1051/0004-6361/201731970

Frebel, A., & Norris, J. E. (2015). Near-Field Cosmology with Extremely Metal-Poor Stars. *Annual Review of Astronomy and Astrophysics*, *53*(1), 631–688. https://doi.org/10.1146/annurev-astro-082214-122423

Getting Started with the Optical Data | SDSS. Retrieved April 20, 2024, from www.sdss4.org website: https://www.sdss4.org/dr17/spectro/spectro_basics/

Gunn, J. E., & Peterson, B. A. (1965). On the Density of Neutral Hydrogen in Intergalactic Space. *The Astrophysical Journal*, *142*, 1633. https://doi.org/10.1086/148444

Heger, A., & Woosley, S. E. (2002). The Nucleosynthetic Signature of Population III. *The Astrophysical Journal*, *567*(1), 532–543. https://doi.org/10.1086/338487

Huyan, J., Kulkarni, V. P., Poudel, S., Tejos, N., Péroux, C., & Lopez, S. (2023). Discovery of Super-enriched Gas ∼1 Gyr after the Big Bang. *The Astrophysical Journal. Letters*, *954*(1), L19–L19. https://doi.org/10.3847/2041-8213/aceefe

Khare, P. (2013). Quasar absorption lines: an overview. *BULLETIN of the ASTRONOMICAL SOCIETY of INDIA*, *41*(1), 41.

Kulkarni, V. P., Fall, S. M., Lauroesch, J. T., York, D. G., Welty, D. E., Khare, P., & Truran, J. W. (2005). *Hubble Space Telescope*Observations of Element Abundances in Low-Redshift Damped Lyα Galaxies and Implications for the Global Metallicity-Redshift Relation. *The Astrophysical Journal*, *618*(1), 68–90. https://doi.org/10.1086/425956

Ledoux, C., Petitjean, P., Fynbo, J. P. U., Møller, P., & Srianand, R. (2006). Velocity-metallicity correlation for high-z DLA galaxies: evidence of a mass-metallicity relation? *Astronomy & Astrophysics*, *457*(1), 71–78. https://doi.org/10.1051/0004-6361:20054242

Maiolino, R., & Mannucci, F. (2019). De re metallica: the cosmic chemical evolution of galaxies. *The Astronomy and Astrophysics Review*, *27*(1). https://doi.org/10.1007/s00159-018-0112-2

Morrison, S. J., Kulkarni, V. P., Som, D., DeMarcy, B., Quiret, S., & Peroux, C. (2016). ELEMENT ABUNDANCES IN A GAS-RICH GALAXY ATz= 5: CLUES TO THE EARLY CHEMICAL ENRICHMENT OF GALAXIES. *The Astrophysical Journal*, *830*(2). https://doi.org/10.3847/0004-637x/830/2/158

Morton, D. L. (2003). Atomic Data for Resonance Absorption Lines. III. Wavelengths Longward of the Lyman Limit for the Elements Hydrogen to Gallium. *Astrophysical Journal Supplement Series*, *149*(1), 205–238. https://doi.org/10.1086/377639

Noterdaeme, P., Petitjean, P., Carithers, W., Pâris, I., Font-Ribera, A., Bailey, S., … Schneider, D. P. (2012). Column density distribution and cosmological mass density of neutral gas: Sloan Digital Sky Survey-III Data Release 9. *Astronomy & Astrophysics*, *547*, L1. https://doi.org/10.1051/0004-6361/201220259

Péroux, C., Dessauges-Zavadsky, M., D'Odorico, S., Kim, T.-S., & McMahon, R. G. (2003). A homogeneous sample of sub-damped Lyman alpha systems - II. Statistical, kinematic and chemical properties. *Monthly Notices of the Royal Astronomical Society*, *345*(2), 480–496. https://doi.org/10.1046/j.1365-8711.2003.06952.x

Pettini, M. (2003). Element Abundances through the Cosmic Ages. *ArXiv Astro-Ph/0303272*. https://doi.org/10.48550/arxiv.astro-ph/0303272

Poudel, S., Kulkarni, V. P., Cashman, F. H., Frye, B., Peroux, C., Rahmani, H., & Quiret, S. (2019). Metal-enriched galaxies in the first ∼1 billion years: evidence of a smooth

metallicity evolution at z ∼ 5. *Monthly Notices of the Royal Astronomical Society*, *491*(1), 1008–1025. https://doi.org/10.1093/mnras/stz3000

Poudel, S., Kulkarni, V. P., Morrison, S. J., Peroux, C., Som, D., Rahmani, H., & Quiret, S. (2018). Early metal enrichment of gas-rich galaxies at z ∼ 5. *Monthly Notices of the Royal Astronomical Society*, *473*(3), 3559–3572. https://doi.org/10.1093/mnras/stx2607

Poudel, S., Kulkarni, V. P., Som, D., & Peroux, C. (2021). Metals and a search for molecules in the distant Universe: Magellan mike observations of sub-DLAs at 2 < z < 3. *Monthly Notices of the Royal Astronomical Society*, *504*(1), 731–743. https://doi.org/10.1093/mnras/stab926

Prochaska, J. X., Gawiser, E., Wolfe, A. M., Castro, S., & Djorgovski, S. G. (2003). The Age-Metallicity Relation of the Universe in Neutral Gas: The First 100 Damped Ly Systems. *The Astrophysical Journal*, *595*(1), L9. https://doi.org/10.1086/378945

Prochaska, J. X., Gawiser, E., Wolfe, A. M., Cooke, J., & Gelino, D. M. (2003). The ESI/Keck II Damped Lyα Abundance Database. *The Astrophysical Journal Supplement Series*, *147*(2), 227. https://doi.org/10.1086/375839

Quiret, S., Péroux, C., Zafar, T., Kulkarni, V. P., Jenkins, E. B., Milliard, B., … Monier, E. M. (2016). The ESO UVES advanced data products quasar sample – VI. Sub-damped Lyman α metallicity measurements and the circumgalactic medium. *Monthly Notices of the Royal Astronomical Society*, *458*(4), 4074–4121. https://doi.org/10.1093/mnras/stw524

Rao, S., Turnshek, D. A., Sardane, G. M., & Monier, E. M. (2017). The statistical properties of neutral gas at z < 1.65 from UV measurements of Damped Lyman Alpha systems. *Monthly Notices of the Royal Astronomical Society*, *471*(3), 3428–3442. https://doi.org/10.1093/mnras/stx1787

Savage, B. D., & Sembach, K. R. (1991). The analysis of apparent optical depth profiles for interstellar absorption lines. *The Astrophysical Journal*, *379*, 245–245. https://doi.org/10.1086/170498

Som, D., Kulkarni, V. P., Meiring, J. D., York, D. G., Peroux, C., Lauroesch, J. T., … Khare, P. (2015). *HUBBLE SPACE TELESCOPE*OBSERVATIONS OF SUB-DAMPED Ly*α*ABSORBERS AT*z*< 0.5, AND IMPLICATIONS FOR GALAXY CHEMICAL EVOLUTION. *The Astrophysical Journal*, *806*(1), 25–25. https://doi.org/10.1088/0004-637x/806/1/25

Tumlinson, J., Peeples, M. S., & Werk, J. K. (2017). The Circumgalactic Medium. *Annual Review of Astronomy and Astrophysics*, *55*(1), 389–432. https://doi.org/10.1146/annurev-astro-091916-055240

Tumlinson, J., Thom, C., Werk, J. K., Prochaska, J. X., Tripp, T. M., Weinberg, D. H., … Sembach, K. R. (2011). The Large, Oxygen-Rich Halos of Star-Forming Galaxies Are a Major Reservoir of Galactic Metals. *Science*, *334*(6058), 948–952. https://doi.org/10.1126/science.1209840

Wolfe, A. M., Gawiser, E., & Prochaska, J. X. (2005). DAMPED LYα SYSTEMS. *Annual Review of Astronomy and Astrophysics*, *43*(1), 861–918. https://doi.org/10.1146/annurev.astro.42.053102.133950

APPENDIX A

OBSERVED SIGHTLINES

Here are the 42 sightlines within wavelength range $3 \lesssim z_{abs} \lesssim 5$ for this project.

Table A.1 The observed Sightlines with Coordinates, redshift of QSO and intervening gas-rich galaxies and column density

S.N.	RAJ2000	DEJ2000	z_{qso}	z_{abs}	$\log N_{H\,I}$
1.	10 34 03.8800	+38 02 48.480	3.567	3.514	20.58
2.	10 50 49.2800	+44 11 44.880	4.310	4.310	20.72
3.	12 00 39.8200	+40 15 56.150	3.333	3.218	20.81
4.	14 46 17.3600	-01 01 31.080	4.168	4.086	20.33
5.	01 33 40.3200	+04 00 59.760	4.172	3.772	20.74
6.	16 02 52.0600	+12 37 04.440	3.486	3.406	20.81
7.	22 44 53.7500	+03 35 23.280	3.364	3.274	20.50
8.	22 49 56.0800	+00 02 18.240	3.308	3.044	20.30
9.	08 11 32.2100	+37 27 55.440	3.828	3.563	20.66
10.	10 15 26.3300	+39 21 07.200	3.605	3.602	20.69
11.	15 02 27.2200	+30 34 52.680	3.332	3.282	20.83
12.	15 06 05.3600	+34 06 35.270	3.984	3.722	21.18
13.	23 11 24.8900	+01 09 52.560	3.429	3.413	21.19
14.	00 07 30.7800	+02 24 35.280	3.559	3.550	21.08
15.	02 55 18.5800	+00 48 47.520	4.006	3.917	21.27
16.	02 56 49.0200	+00 18 57.240	3.850	3.737	21.03
17.	08 13 08.7100	+39 10 52.680	3.430	3.366	21.19
18.	09 48 02.4900	+43 07 14.170	3.728	3.487	21.04
19.	10 18 21.1900	+00 01 53.400	3.477	3.406	21.09
20.	11 49 00.3500	+01 53 58.200	3.367	3.310	21.10
21.	12 17 08.6000	+03 40 11.640	3.902	3.786	21.36
22.	13 05 02.2800	+05 21 51.120	4.076	3.679	21.17
23.	13 05 53.3000	+06 43 47.280	4.047	3.958	21.32
24.	14 45 12.2000	+30 08 49.560	3.506	3.261	21.23
25.	15 28 07.1900	+32 54 56.160	3.638	3.474	21.34
26.	16 10 00.4300	+14 16 24.600	3.889	3.717	21.14
27.	16 48 10.0800	+26 02 11.400	3.351	3.255	21.27
28.	23 09 52.2900	-00 31 39.000	3.96	3.731	21.34
29.	01 55 45.5700	+10 00 20.520	4.122	4.062	20.58
30.	07 47 49.7400	+44 34 17.040	4.435	4.019	21.05
31.	11 35 34.5500	+34 44 33.720	4.030	4.028	20.46
32.	14 21 03.8300	+34 33 32.040	4.960	4.657	20.73
33.	14 21 03.8300	+34 33 32.040	4.960	4.795	20.36
34.	16 07 34.2200	+16 04 17.400	4.760	4.471	20.61
35.	01 53 05.0900	-01 51 36.000	3.715	3.390	20.55
36.	02 46 22.1900	+04 10 30.360	3.548	3.266	20.55
37.	08 21 59.5900	+40 22 36.480	3.770	3.611	20.53
38.	12 03 59.0700	+34 11 14.290	3.756	3.685	20.92
39.	13 50 04.8800	+36 00 45.360	3.577	3.302	20.49
40.	15 28 56.2800	+15 04 52.320	3.411	3.233	20.50
41.	21 23 57.5700	-00 53 49.920	3.637	3.626	20.53
42.	23 22 30.1700	+00 12 31.320	3.536	3.348	20.63

APPENDIX B
NULL GEODESICS IN FRW METRIC

Friedmann-Robertson-Walker (FRW) metric is a mathematical description of the expanding universe in the framework of Einstein's general relativity given as (Gunn & Peterson, 1965);

$$ds^2 = dt^2 - a(t)^2\left[\frac{dr^2}{1-kr^2} + r^2(d\theta^2 + \sin^2\theta d\varphi^2)\right] \quad (B.1)$$

where k is the curvature parameter and $a(t)$ is the dimensionless scale factor of expansion. For photon travels in a FRW metric, i.e., null geodesic; which plays a crucial role in cosmology because it allows us to observe and study the distant parts of the universe, by studying the behavior of light, we can determine the curvature and expansion of the universe, therefore

$$ds^2 = 0 \quad (B.2)$$

When Photon travels radially or radial null geodesic in an equatorial plan then the Equation B.1 becomes

$$dt^2 = a(t)^2\left[\frac{dr^2}{1-kr^2}\right] \quad (B.3)$$

For the crest of a photon wave emitted from some galaxy at a distance $r = r_1$ and time $t = t_1$ and reaching us at $r = 0$ and $t = t_0$, we can write

$$\int_{t_1}^{t_0}\frac{dt}{a(t)} = \int_{r_1}^{0}\frac{dr}{\sqrt{1-kr^2}} \quad (B.4)$$

Now, if wavelength of the emitted light is λ_{rest} and the of the observed light is λ_{obs}, then the subsequent wave crest departs from the same galaxy at time $t_1 + (\lambda_{rest}/c)$ and arrives at the observer's location at time $t_0 + (\lambda_{obs}/c)$. Therefore,

$$\int_{t_1+(\lambda_{rest}/c)}^{t_0+(\lambda_{obs}/c)}\frac{dt}{a(t)} = \int_{r_1}^{0}\frac{dr}{\sqrt{1-kr^2}} \quad (B.5)$$

Subtracting Equation B.4 from B.5 with assuming $a(t)$ remains unchanged then,

$$\int_{t_1+(\lambda_{obs}/c)}^{t_0+(\lambda_{obs}/c)} \frac{dt}{a(t)} - \int_{t_1}^{t_0} \frac{dt}{a(t)} = 0 \tag{B.6}$$

$$\int_{t_1}^{t_0} \frac{dt}{a(t)} + \int_{t_0}^{t_0+(\lambda_{obs}/c)} \frac{dt}{a(t)} - \int_{t_1}^{t_1+(\lambda_{obs}/c)} \frac{dt}{a(t)} - \int_{t_1}^{t_0} \frac{dt}{a(t)} = 0 \tag{B.7}$$

Here, for small time interval $\delta t = \lambda/c$ we obtain,

$$\frac{\delta t_{obs}}{a(t_0)} = \frac{\delta t_{rest}}{a(t_1)} \tag{B.8}$$

$$\frac{a(t_0)}{a(t_1)} = \frac{\lambda_{obs}}{\lambda_{rest}} \tag{B.9}$$

The Doppler redshift to the spectral line due to motion is given by,

$$z = \frac{\Delta\lambda}{\lambda} \tag{B.10}$$

Then,

$$z = \frac{\lambda_{obs} - \lambda_{rest}}{\lambda_{rest}} \tag{B.11}$$

The cosmological redshift is something different, although we are often referring to it in the same terms of the doppler redshift. Cosmological redshift is actually due to expansion of spacetime itself. Observationally, redshift refers to the extent by when a photon from an object travel to an observer, its wavelength moves toward the red end of the spectrum. In relation to cosmology, redshift serves as parameter representing expansion of Universe. Therefore, cosmological redshift in FRW metric represent by comparing equation B.9 and B.11,

$$\frac{a(t_0)}{a(t_1)} = (1 + z) \tag{B.12}$$

$$\therefore \lambda_{obs} = \lambda_{rest}\,(1 + z) \tag{B.13}$$